Hardness modelling of porous copper bodies

Hugo Miguel Vicente Cardoso

Thesis to obtain the Master of Science degree in

Materials Engineering

Supervisors:

Professor Alberto Eduardo Morão Cabral Ferro

Professor Ricardo Miguel Gomes Simões Baptista

Examination Committee

Chairperson: Professor Pedro Miguel Gomes Abrunhosa Amaral

Supervisor: Professor Alberto Eduardo Morão Cabral Ferro

Member of the Committee: Professor Augusto Manuel Moura Moita de Deus

November 2017

Declaração

Declaro que o presente documento é um trabalho original da minha autoria e que cumpre todos os requisitos do Código de Conduta e Boas Práticas da Universidade de Lisboa

Declaration

I declare that this document is an original work of my own authorship and that it fulfills all the requirements of the Code of Conduct and Good Practices of the Universidade de Lisboa.

Resumo

Pós de cobre esféricos são essenciais nos processos de manufactura aditiva de componentes metálicos. Estes processos requerem um elevado escoamento resultante da esfericidade das partículas. Além disto, componentes obtidos a partir de pós podem apresentar porosidade residual ou porosidade controlada. Os testes de dureza permitem avaliar a resistência de corpos metálicos a deformações plásticas que dependem da porosidade da peça.

Os principais objectivos deste trabalho são propor um modelo de dureza dependente da porosidade, usando o método dos elementos finitos (MEF), e desenvolver um método de esferoidização de pós que permita a criação de corpos com porosidade controlada. Para o primeiro caso, foi simulado um teste de dureza Brinell em corpos de cobre puro. Para o segundo caso, pós de cobre electrolíticos (dendríticos) foram submetidos a um processo de esferoidização no estado líquido.

Os pós de cobre foram esferoidizados num forno de resistência de grafite, sob vácuo, num leito de grafite em pó, num molde de grafite, segundo uma abordagem de fusão in situ. As variáveis analisadas foram: temperatura, tempo de permanência, peso aplicado e fracção mássica de cobre-grafite. Os dois pós utilizados foram separados numa solução aquosa de ácido clorídrico aquecida. As amostras foram caracterizadas por MEV e EDS. Verificou-se que as partículas esferoidizadas numa mistura com grafite do tipo KS4, com uma proporção de cobre-grafite de 1:1, a 1100ºC durante 30 minutos, sob uma pressão reduzida, obtiveram os melhores valores relativos ao factor de forma (1.55±0.46).

Realizaram-se simulações de ensaios de dureza, pelo MEF, para estudar a influência da porosidade e do rácio carga/diâmetro do indentador (F/D^2) na dureza Brinell. O corpo poroso de cobre foi criado de acordo com o modelo GTN. Obteve-se uma relação linear entre a dureza de Brinell e a porosidade do corpo. Para cobre, com uma fracção volúmica de poros entre 0 e 0.1, os resultados da simulação da dureza Brinell podem ser escritos numa só equação, $BHN = 74{,}9 \cdot (F/D^2)_h{}^{-0{,}065} - 187{,}7 \cdot VVF \cdot (F/D^2)_h{}^{-0{,}215}$, em que ($F/D^2$) é o rácio $F/10D^2$ adimensional e VVF a fracção volúmica de poros. Ocorre densificação do corpo poroso na região de indentação. Verificou-se a ocorrência de “pile-up”, sendo este máximo para um rácio F/D^2 de 10 kgf/mm² num corpo com 0% de porosidade.

Palavras-chave: pós esféricos; cobre; grafite; método dos elementos finitos; dureza; porosidade

Abstract

Spherical powders are essential for additive manufacturing of metallic components. These processes require high powder flowability provided by particles with spherical shape. Also, powder made components are prone to develop residual porosity or can be developed with controlled porosity. Hardness testing is a rapid tool to access resistance to plastic flow of metallic materials. This resistance depends on component porosity.

This work proposes to model the hardness dependence on porosity using finite element experiments. It also proposes a method to develop spherical powders usable to produce model materials with controlled porosity. Pure copper and Brinell hardness testing were selected for the FEM experiments. Electrolytic dendritic copper powders were select for the liquid metal spheroidization process.

Spheroidization was carried out using a non-wettable graphite powder bed, using an in situ melting solidification process. Copper powders were heat treated in a primary vacuum furnace using a graphite powder bed and graphite dies. The analysed variables were temperature, holding time, copper/graphite mass ratio (CGR) and applied stress. Copper was separated from the mixture using a warm hydrochloric acid aqueous solution. The samples were characterized by SEM and EDS. The best spheroidization shape factor, 1.55±0.46, was achieved for copper powders processed at 1100ºC for 30 minutes, with low applied stress, in a mix with graphite KS4 and a CGR of 1:1.

FEM simulations were carried out to study the influence of porosity and load/indenter size ratio, F/D² ratio, on materials hardness. The GTN model was used to simulate a porous copper body. A direct linear relationship was observed between Brinell hardness and relative density. For copper, and for a void volume fraction (VVF) between 0 and 0.1, Brinell hardness simulation results can be expressed in a single equation, $BHN = 74{,}9 \cdot (F/D^2)_h^{\,-0{,}065} - 187{,}7 \cdot VVF \cdot (F/D^2)_h^{\,-0{,}215}$, where $(F/D^2)_h$ is the F/10D² dimensionless ratio and VVF the void volume fraction. Both densification, in the region beneath the indenter, and pile-up, at the periphery of the indentation, were observed. Pile-up was maximum for a 10 kgf/mm² F/D² ratio and 0% porosity.

Keywords: spherical powders; copper; graphite; finite element method; hardness; porosity

Agradecimentos

Primeiro que tudo, ao meu orientador, Professor Alberto Ferro, agradeço o convite que me fez para a realização deste trabalho, pela confiança e exigência que sempre me transmitiu, pela sua ajuda e pela metodologia de trabalho que me ensinou durante este curso.

Ao Professor Ricardo Baptista agradeço todo o apoio e orientação que me transmitiu durante esta jornada, em particular o seu conhecimento sobre modelação que se revelou inestimável neste trabalho.

Dirijo também um agradecimento à Professora Fernanda Margarido pela ajuda que foi para mim neste trabalho, particularmente com o método de separação de pós, e pela sua disponibilidade.

Um agradecimento especial ao Tomás Seixas, por toda a ajuda que foi para mim durante a esta tese e pelo exemplo de excelência.

Agradeço ao Professor Rui Silva e ao Doutor Filipe Oliveira, da Universidade de Aveiro, a disponibilidade de utilização dos equipamentos do Departamento de Engenharia de Materiais e Cerâmica, bem como a ajuda que me providenciaram na realização dos ensaios experimentais.

Agradeço também aos meus amigos que durante esta caminhada me ajudaram, à Rita, ao Miguel, ao João, à Joana, ao André, ao Guilherme, ao André, e em particular à Madalena Garcia, por todo o apoio, pela incrível paciência que teve comigo, pelo ânimo, força, amizade e cumplicidade, muito obrigado.

Finalmente, e com grande orgulho, agradeço à minha família por tudo o que me proporcionaram, que me permitiu chegar onde hoje estou. Aos meus avós, José e Celeste, obrigado pelos ensinamentos, valores e força que sempre fizeram chegar até mim. Aos meus tios, Nuno e Maria João, obrigado pela ajuda que sempre me deram, o apoio e a força. Ao meu primo, Tiago, obrigado pela simplicidade e carinho. Ao meu irmão, Gonçalo, obrigado por me aturares, mas acima de tudo por me deixares ser um exemplo para ti, em todos os sentidos. Aos meus pais, José e Conceição, pelo exemplo de persistência que foram para mim, e por tudo o que me deram, obrigado.

Hugo

Acknowledgments

First and foremost, to my supervisor, Professor Alberto Ferro, I thank the invitation for this work, for the trust and demand you have always given me, for your helping hand and for the methodology of work you taught me during this course.

To Professor Ricardo Baptista, I thank all the support and guidance given to me during this journey, especially the knowledge about modelling that proved to be invaluable in this work.

I'd like to thank Professor Fernanda Margarido for all the help with the separation methods, and for all the time spent helping me.

A special thanks to Tomás Seixas, for all the help he has given me during this thesis and for his example of excellence.

I thank Professor Rui Silva and Dr. Filipe Oliveira, from the University of Aveiro, for the availability of equipment from the Department of Materials and Ceramics Engineering, as well as the help they provided me during the experimental tests.

I also thank my friends who, during this walk, helped me always: to Rita, Miguel, Joao, Joana, André, Guilherme, André, and in particular Madalena, for all the support, incredible patience with me, by the spirit, strength, friendship and complicity, thank you very much.

Finally, and with great pride, I thank my family for everything they have given me, which allowed me to get where I am today. To my grandparents, José and Celeste, thank you for the teachings, values and strength that always made me come. To my uncles, Nuno and Maria João, thank you for the help you have always given me, the support and the strength. To my cousin, Tiago, thank you for the simplicity and affection. To my brother, Gonçalo, thank you for your attention, but above all for letting me be an example for you, in every way. To my parents, Jose and Conceição, for the example of persistence that they were for me, and for all that they gave me, thank you.

Hugo

Contents

List of Figures

List of Tables

Acronyms

BC – Boundary conditions

CAX4R – 4-node bilinear axisymmetric quadrilateral, reduced integration, hourglass control

C3D8R – 8-node linear brick, reduced integration, hourglass control

CF – Concentrated force

CGR – Copper-graphite ratio

CP – Contact pressure

CPM – classical plasticity model

DT – Dwell time

GTN – Gurson-Tvergaard-Needleman

EU – European Union

EDS – Energy dispersive spectroscopy

F/D² ratio – Force-Diameter ratio

FEM – Finite element method

BHN – Brinell hardness number

LS – Liquid/Solid

LV – Liquid/Vapor

EPS – Equivalent plastic strain

PM – Powder metallurgy

VVF – Void volume fraction

VVFG – Void volume fraction due to void growth

SEM – Scanning electron microscopy

SE – Secondary electron

SV – Solid/Vapor

WD – Working distance

Symbols

α – temperature coefficient of resistivity

γ – surface tension

$\dot{\varepsilon}$ – strain rate

ε_p – equivalent plastic strain

ρ – specific electrical resistivity

θ - contact angle

σ – equivalent stress

λ – thermal conductivity

μ – friction coefficient

μm – micrometer

ºC – Celsius degrees

d_{10} – diameter for which 10% of the particles have lower diameter, in volume

d_{50} - diameter for which 50% of the particles have lower diameter, in volume

d_{90} - diameter for which 90% of the particles have lower diameter, in volume

E_f – shape factor

E – Young or Elastic modulus

kgf – kilogram force

MPa – Mega pascal

wt% - weight percentage

1. Introduction

Numerous industrial applications where metal powders play a key role require particles with increasingly better flowability for processes where this parameter is critical, such as additive manufacturing and metal powder injection. These powders are better suited for the production of parts with controlled porosity than other produced by water atomization or electrolysis, facilitating the experimental validation of numerical simulation models.

The present work has two main goals: study and optimize a powder spheroidization process (liquid-solid method) through the use of a graphite powder bed that promotes local non-wettability regions between copper and graphite; serve as an introduction to the use of the finite element method (FEM) for hardness test simulations. The capabilities of this method can be useful to predict and explain experimental results in both dense and porous materials. Working with a model that successfully recreates reality also provides a reliable background for the development and improvement of constitutive equations for plastic flow in porous materials.

This work was structured into three parts. The first part studies the production of spherical copper powders from dendritic powders. The second part relates to the characterization of the spherical copper powders. The last part concerns the FEM study of the hardness test and comparison is made between a pore-free and a porous copper material.

This thesis is divided into 6 sections. The present introduction is section 1. Section 2, State of the Art, is where literature on copper powder production methods, spherical powder production and applications, hardness tests and FEM modelling is reviewed. Section 3, Experimental methods and techniques, presents the experimental methods and techniques as well as the materials used in this work. Section 4, Experimental results and discussion, presents the experimental results and the analysis of the spheroidization process. On section 5, Modelling, the parameters and set-up for the creation of the computational model are presented together with the simulation results. Section 6, Conclusions, offers a compilation of both the experimental and computational results and the final conclusions, along with suggestions on further developments.

2. State of the Art

In this chapter, the properties, production methods and applications of copper powders are introduced, as well as the processes of spheroidization of these powders. The hardness test modelling is reviewed, with detail given to the Finite Element Method.

2.1. Copper

Copper is a metallic material with high thermal and electrical conductivity which stands atop many other materials as reported in Table 1 [1]. This, coupled with its effectiveness as a catalyst, resistance to corrosion and good strength and fatigue resistance [2][3] makes copper a sought after material for several applications, which includes electrical components, filters, brushes, catalysts and structural parts [1][2][4].

Table 1 - Comparison between materials used in electrical contacts in terms of electrical, thermal and mechanical properties [1]**.**

Material	Density (g/cm^3)	ρ (10^{-8} Ωm)	λ (W/(mºC))	E (GPa)
Copper	8.9	1.75	380	120
Gold	19.3	2.3	310	84
Silver	10.5	1.65	418	75
Platinum	21.4	11.7	70	154
Tungsten	19.3	5.5	190	350
Iron	7.8	10	60	200
Aluminium	2.7	2.9	210	72
Graphite	1.8	700	160	3

2.1.1. Copper Powders

Metal powders are defined as metals or alloys in the form of particles, with sizes usually smaller than 1 mm [5]. Powder metallurgy (PM) enables the mass production of metallic parts with a near-net shape at a low cost, without the defects associated with traditional metallurgical processes such as casting, like blow holes, shrinkage and inclusions [4][6].

The first copper powder metallurgy parts date back to the early 1920's with bronze self-lubricating bearings being used in the automotive industry. In the 1930's the production of electrolytic copper powders enabled the development of copper-graphite electrical brushes. With the advents of the Second World War and the consequent development of the metallic industry, copper powder production had

another surge with the metal being added for alloy strengthening [4]. Nowadays, the main consumers of PM parts are the automotive industries, followed by the electronics industry sector.

In 2014, the European Commission reported that the turnover of PM parts was over 6 billion euros per year. The same document identifies the sectors addressing the development needs for research on the topic: transportation, electronics, energy, consumer goods and tooling. The mid-term objective for the EU (for 2020) is set on powder processing and metallurgy, while the long term vision (2050) is set on the development of suitable powders for additive manufacturing [7]. The market size of this area of PM is predicted to grow at an average rate of 23% until 2025, as shown in Figure 1 [8].

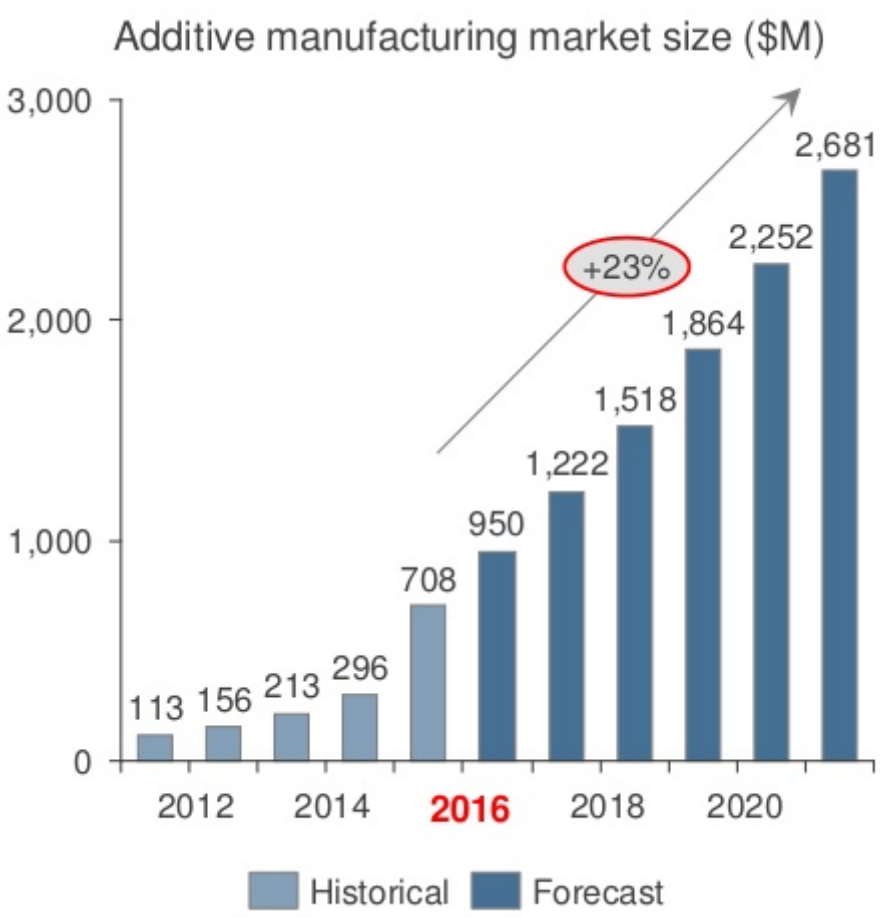

Figure 1 – Additive manufacturing market growth forecast for 2025 showing the demand for powders that suit this process [8]**.**

With such a revenue forecast for the upcoming years, driven by the need of the industries related with the energy sector, research on copper powders and its applications is an area of increasingly greater interest.

2.1.2. Copper powder production methods

The main copper powder production methods are atomization, oxide reduction, hydrometallurgy and electrolysis. The starting powders used in this work were produced by electrolysis and for this reason, this specific process will be the focus of this section.

The production of powders by electrolysis is a processing method with low capital investment and operational costs. It yields high purity powders when compared with other methods, with copper composition ranging from 99.1 to 99.8 wt%, and oxygen content ranging from 0.1 to 0.8 wt% [4].

Table 2 – Comparison between different copper production methods with respect to composition and powder morphology.

Type of powder	Composition (wt%)		Powder Morphology
	Copper	Oxygen	
Electrolytic	99.1-99.8	0.1-0.8	Dendritic
Oxide reduced	99.3-99.6	0.2-0.6	Irregular
Water reduced	99.3-99.7	0.1-0.3	Irregular to spherical

Table 2 shows a comparison between the major processes utilized in the production of copper powders.

Copper electrolysis is carried out in an electrolytic bath on which an electric current is applied between an anode and a cathode. The anode is connected to the positively charged pole whereas the cathode is connected to the negatively charged pole. Copper oxidation will occur at the anode, with consequent production of copper ions (Cu^{2+}) that will migrate across the electrolyte towards the cathode. At the cathode, copper ions will be reduced. As a consequence, powders are deposited on the cathode, and are later removed with a brush [6]. The reactions on each of the poles are described by equations (1) (anode reaction) and (2) (cathode reaction) [9].

$$Cu \rightarrow Cu^{+2} + 2e^{-} \quad (1)$$

$$Cu^{+2} + 2e^{-} \rightarrow Cu \quad (2)$$

The distance between the anode and the cathode influences the size and amount of powders produced. When the distance increases the particle's size increases. However, increasing the distance between the anode and the cathode leads to a lower amount of copper particles [9].

The electrolytic bath consists of copper sulphate, sulphuric acid (provides hydrogen ions that improve bath conductivity) and distilled water [9]. The anode is usually made of electrolytically refined copper, and the cathode of a lead alloy sheet [4].

Table 3 - Typical conditions for the production of electrolytic copper powder [4]**.**

Parameter	Value
Copper concentration	5-15 g/L
Sulphuric acid concentration	150-175 g/L
Temperature	25-60 ºC
Anode current density	430-550 A/m^2
Cathode current density	700-1100 A/m^2
Cell potential	1.0-1.5 V

The typical conditions employed in the production of electrolytical grade copper powders are specified in Table 3. The parameters detailed in the table are the ones which most influence the produced powder's properties.

Copper powder production is favoured by low electrolytic copper ion concentration, and high acid content. At higher electrolyte temperatures the powders become coarser and the current efficiency is increased, which causes a drop in terms of cell voltage [4].

Studies on the effects of process parameters indicate that powder's size increase with removal time and the increase in distance between the anode and the cathode; a current density increase leads to powders with lower sizes [9]. Copper powders produced by electrolysis exhibit a dendritic morphology at the end of the process.

2.2. Wettability and surface tension

Liquids tend to adopt shapes that minimize their surface area, so that the maximum number of atoms are in the bulk interacting with neighbours. Therefore, in the absence of gravity, droplets tend to be spherical, since a sphere is the shape with the smallest surface-to-volume ratio. The resulting area-reduction phenomenon leads to the concept of surface tension (γ) which is the work needed to change the surface area of a sample by an infinitesimal amount [10].

The surface tension of a liquid can be measured with many methods. One of them, the sessile drop method allows for the measurement of surface tension of liquid by applying Young's equation for the balance between interfaces. In this method, a liquid drop is placed on a flat substrate and its profile image is acquired [11]. The contact angle (θ) obtained from the profile image will be used to calculate the surface tension.

The contact angle (θ) derives from a balance of surface tensions between solid-vapor (γ_{SV}), solid-liquid (γ_{SL}) and liquid-vapor (γ_{LV}) interfaces, according to the Young equation (3) [12][13].

$$cos\theta = \frac{\gamma_{SV} - \gamma_{SL}}{\gamma_{LV}} \quad (3)$$

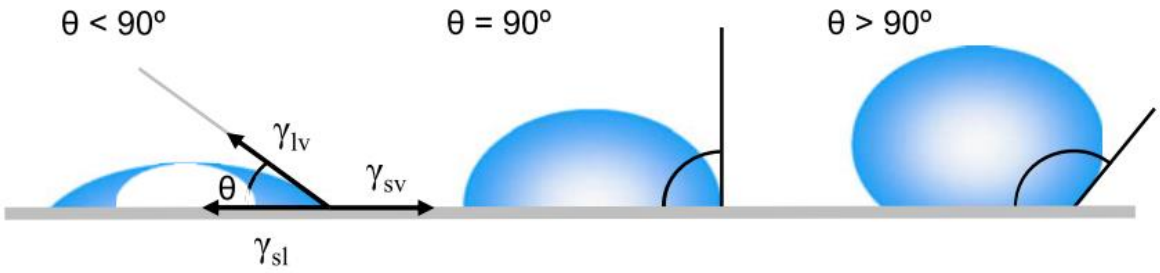

Figure 2 – Droplet morphology variation with contact angle [14]**. Example of the sessile drop method.**

A liquid is said to fully wet a solid when its contact angle is zero, with the liquid spreading over the solid. If the contact angle is higher than 90 degrees, the liquid will ball-up thus not wetting the surface [12], as depicted in Figure 2 [14].

2.3. Spherical Powders

The development of powder metallurgy, three-dimensional printing and metal injection moulding has led to a specific need for spherical powders, with fine particle size and smooth particle surface. The powder's shape and reduced size allow for a better compaction and therefore a better densification when sintering [15]. These benefits prompt increasing demand of spherical powders for part production. In order to mass produce spherical powders it is necessary to control the particle's size distribution and process reproducibility [16].

Spherical particles can be produced by several processes. Gas atomization is a method that allows for fine grain size, spherical and clean (low oxygen content) particles. In this production method, a liquid metal stream is disintegrated by means of a impinging jet of gas (usually argon or nitrogen) [17][18]. Despite providing spherical particles, price is still an obstacle to more widespread use, due to labour costs and plant capacity [19]. This presents an opportunity for the development of a process that allows one to obtain spherical powders with lower adjacent costs with no further add-ons to the process.

An approach proposed by Zhenzhi Cheng et al [20] rests on the principles of non-wettability. It consists on using a powder bed of graphite to separate the metallic particles, preventing contact between them. By surrounding the copper particles with graphite platelets it is possible to create a local region where the spheroidization will occur [15], [21], [22]. This method is depicted in Figure 3, and was named LS, liquid-solid method, by the authors [23].

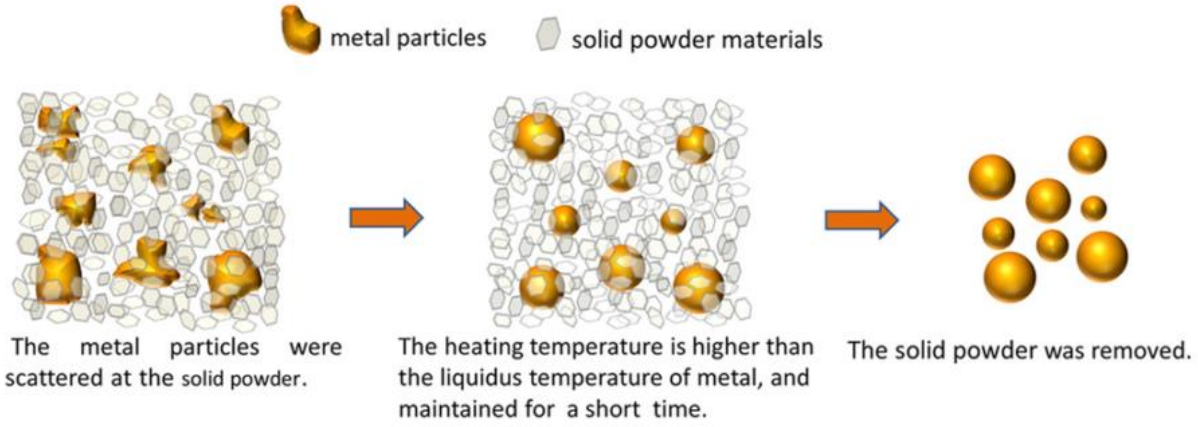

Figure 3 - LS spherical powder formation by making use of a graphite powder bed to promote non-wettability regions around each particle [20]**.**

Graphite's surface energy, at temperatures between 1000 and 2000 K varies from 25 to 95 mJ/m² [24]. As for liquid copper, for temperatures ranging from 1375 to 1525 K, its surface energy is over ten times that of graphite, ranging from 1358 to 1243 mJ/m², respectively [11][25][26]. The wettability of carbon by copper and its alloys show a contact angle of approximately 135º [27], establishing that there is no wetting behaviour between them. Introducing the previously presented parameters in equation (3) theoretically predicts the non-wetting behaviour.

The LS method takes advantage of the low wettability of the Cu-Graphite solid-liquid interface [20]. Results show complete spheroidization of the initial particles, with a particle's size growth up to twice the initial diameter, and few to none impurities (with oxygen content of only 0.048 wt%) [20]. As for carbon impurities low values were recorded, 0.0053 wt%, which is supported by the fact that this element has low solubility in copper [28].

2.4. Modelling

2.4.1. Finite Element Model

ABAQUS (the software used in this project) enables self-learning and allows for autonomous work on numerical modelling. Nonetheless, it is important to understand the theoretical background behind the Finite Element Method. By doing so, it is possible to better understand the results and issues related to the use of the software.

The Finite Element Method, as proposed by Reddy, has three fundamental steps which are: dividing the whole domain into parts; seeking an approximation to the solution as a linear combination of nodal values and approximation functions, and deriving the algebraic relations among the nodal values of the solution over each part and, finally, assembling the parts and obtain the solution to the whole [29].

The domain's discretization rests on the premise of dividing the domain into a collection of geometrical subdomains known as finite elements. This is called a mesh and must represent the problem's geometry. For each element in this mesh, several points called nodes are defined, usually at the vertices, as it is seen in Figure 4.

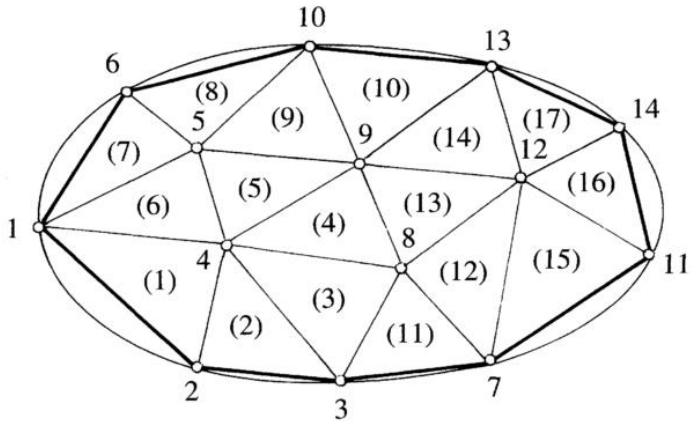

Figure 4 - Discretization of a two-dimensional domain into finite elements. The elements are represented by the numbers between brackets. At the intersection of multiple elements lie the nodes [30]**.**

The functions under consideration over the whole domain are calculated at the nodes, using the problem's governing equations, by a process called interpolation. Lastly, the local solutions of the equations are assembled together within their original positions in the mesh. This section of the problem's resolution has its ground on the continuity between elements and is also subjected to initial conditions as well as boundary conditions [29][30].

2.4.2. Hardness Test Modelling

Indentation hardness tests, such as the Brinell hardness test, are used extensively in industry. Usually carried out on metallic materials, hardness tests can provide information such as tensile strength, wear resistance, ductility and other material's properties [31].

The Brinell hardness test consists on lowering a tungsten carbide ball indenter into the surface of the material under study, in two steps. During the first step, the load is applied and kept for a designated time, after which it is removed. The second step comprises the measurement of two diameters, orthogonal to each other. The hardness number, BHN, is obtained from the mean of the measured diameters, *d*, through equation (4), where F is the applied load in kgf and D is the spherical indenter diameter in mm [31][32]. The equation relates the applied load (F) with the surface area of indentation ($\frac{\pi}{2}D\left(D-\sqrt{D^2-d^2}\right)$.

$$HBW = \frac{2F}{\pi D\left(D-\sqrt{D^2-d^2}\right)} \quad (4)$$

Hardness test modelling, in general, enables the verification and validation of constitutive models and the prediction of material properties without the need to fully test them.

During the initial increments of applied load of the test the deformed region where the material is indented is within the elastic regime. With the load increase of the load, the material will enter the plastic deformation stage.

The propagation of the plastic region is influenced by material's work hardening, as more and more dislocations intersect at the indentation region [33]. If subjected to uniaxial loading, the deformation behaviour, observed by the stress-strain curve, can be assumed to follow a power law like the one in equation (5), with *k* and *n* being material's properties [34].

$$\sigma = k\varepsilon^n \tag{5}$$

Therefore, it is to be expected that the mean contact pressure increases due to work hardening. At the end of the test, the region that was under the indenter is now fully plastic [34].

The relationship between indentation load and diameter presented in equation (6), was empirically developed by Meyer and later referred to by Grau et al [35].

$$F = K\left(\frac{d}{D}\right)^n \tag{6}$$

The same work provided the mean pressure relationship presented in equation (7), which relates the applied load with the indented diameter's projected area, also known as Meyer's hardness for ball indentation [35], which actually is a projected area hardness [36].

$$P = \frac{F}{\pi d^2/4} \tag{7}$$

Detailed studies on contact mechanics involves mathematical complexities which can be solved with the FEM. Bhattacharya and Nix have successfully predicted the response of a material with respect to relationship between hardness, yield stress and the material's Young modulus [37], with simple constitutive equations.

FEM simulations in materials under conditions of compressive load, namely spherical hardness indentation, have been carried out by some researchers. Chen et. al. applied the Gurson model to describe the porosity densification under the indenter, acknowledging the use of this model when assessing contact damage [38]. The Gurson model suggests a damage mechanics material model based on the observation that available plasticity models such as the Von Mises' were predicting incompressibility, even though ductile fracture may involve significant porosity [39].

The same model was used with porous ceramic films, revealing good agreement between the experimental and numerical data regarding the estimation of the uniaxial yield stress of the porous material [40].

Through analysis of FEM on porous copper-matrix composites, Sabzevari et. al. showed that simulation can be successfully utilized to predict and describe the material's behaviour under compressive loads [41], as discussed before, with the possibility to employ different levels of porosity, between 20% and 60%.

2.4.3. Constitutive equations for hardness testing in porous materials

The hardness test can be defined as a static or quasi-static process. Since this work's motivation is to address hardness in porous metallic bodies, it is necessary to create a model that takes it into consideration. The process requires the definition of constitutive equations for both the elastic and plastic regime.

For isotropic materials, the elastic regime requires properties to create the material model, such as density, Young's modulus and Poisson's ratio.

The plastic regime is created with common plastic deformation models from uniaxial testing. However, since the model must account for porosity within the metallic body, the latter model for plastic deformation is incomplete. One appropriate model that successfully completes the latter is the Gurson-Tvergaard-Needleman (GTN) experimental model. It was proposed by Gurson and was later modified by Tvergaard and Needleman to the present form [39][42].

$$\Phi = \left(\frac{\sigma_{eq}}{\sigma_y}\right)^2 + 2q_1 f \cosh\left(-q_2 \frac{3p}{2\sigma_y}\right) - (1 - q_3 f^2) \tag{8}$$

Equation (8) represents the yield surface and plastic potential (Φ) as a function of the void volume fraction (f), where σ_{eq} is the effective Von Mises stress, p the hydrostatic pressure, σ_y the yield stress of the fully dense material and q_1, q_2 and q_3 the Tvergaard empirical material parameters. When $f = 0$, the model is reduced to the Von Mises yield condition.

3. Experimental methods and techniques

In this section, the techniques used to produce and characterize the samples are presented, along with the specimen's identification nomenclature.

3.1. Powder spheroidization

As described in section 2.3, the spheroidization process requires the use of a powder bed (medium). The powder bed and the mould parts are made of graphite, therefore creating a copper-graphite system. Different copper-graphite mass ratios (CGR) were tested: 1:4; 1:2; 1:1 and 2:1. Capillarity effects were compensated with the use of weight on top of the moulds, thus avoiding particle coalescence. The mould and weight design are described in section 3.1.2.

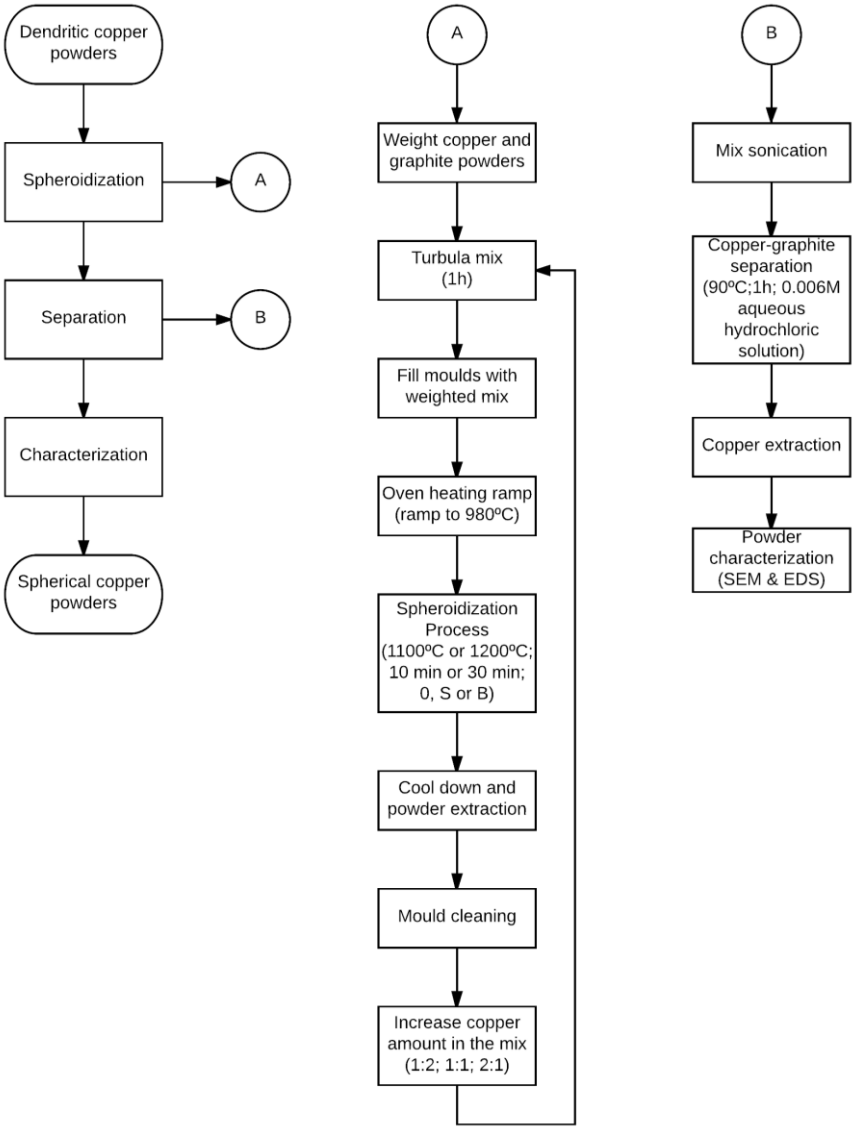

Figure 5 - Experimental procedure flowchart

The experimental procedure flowchart is shown in Figure 5. This procedure is composed of two main processes: Spheroidization and separation, represented by the flowchart sections A and B, respectively.

The copper and graphite powders were weighted and placed inside a Turbula vial and mixed for 1 hour. A quantity of approximately 0.26 g of powder mix was weighted and placed inside the mould. This process was repeated for the two types of graphite, and, each time, more copper powder was added to the mix to increase the CGR to the desired values stated before. The starting mass ratio was 1:4.

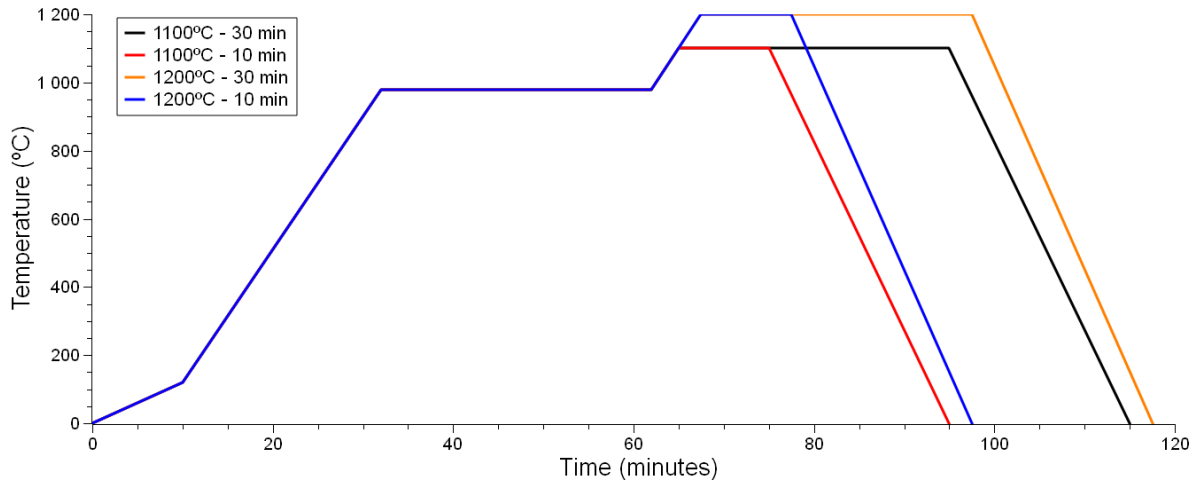

Figure 6 - Spheroidization process thermal cycles applied for all the carried-out tests.

Under primary vacuum, the copper-graphite system was first heated to 980ºC, at a rate of 40ºC per minute and then subjected to two different temperatures independently: 1100ºC and 1200ºC; and two different time periods: 10 and 30 minutes. Figure 6 shows the holding time and temperatures for the different cycles.

After the high temperature stage, the moulds cooled down to 50ºC inside the furnace and were then removed to cool to room temperature.

After removing the samples, all the mould's components and the employed weights were cleaned with ethanol and allowed to dry before repeating the procedure.

The copper-graphite powder blend was mixed using a Turbula T2C from Willy A. Bachofen, with a maximum capacity of two litres.

The spheroidization process was carried out in a Thermal Technology's Model 1000, with a high-density graphite resistance element. All the runs were carried out under primary vacuum of the order of 1 Pa.

3.1.1. Materials

The spheroidization process involves both copper and graphite powders. The starting metallic powder was electrolytic copper powder from Pometon. Figure 7 shows the dendritic morphology of the starting copper powders. According to the manufacturer's information, more than 98wt% of the particles have dimensions up to 63μm and in terms of chemical properties, the supplier ensures a copper weight percentage over 99.7%, with oxygen impurities around 0.08wt%.

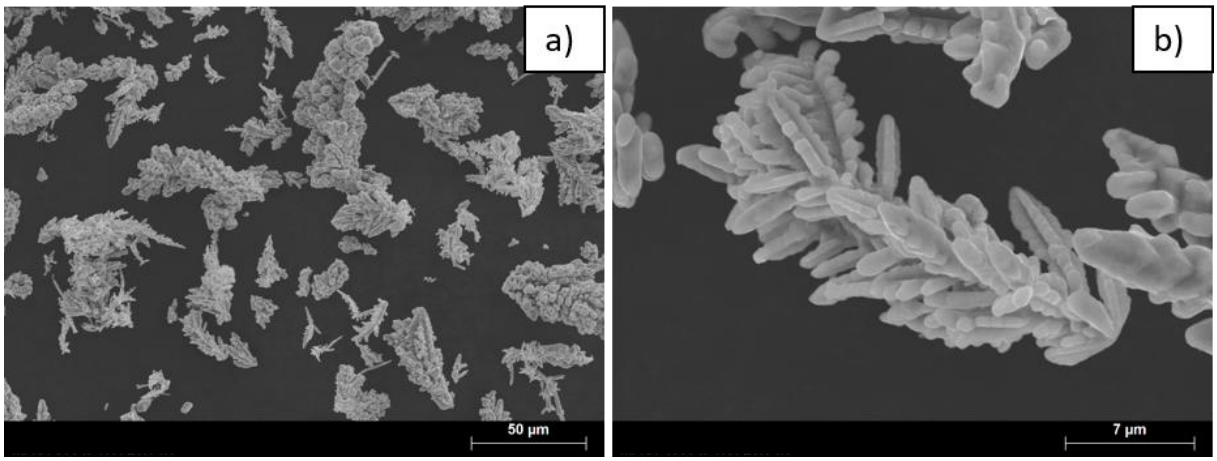

Figure 7 - SEM micrographs of the initial dendritic copper powder used in the spheroidization process.

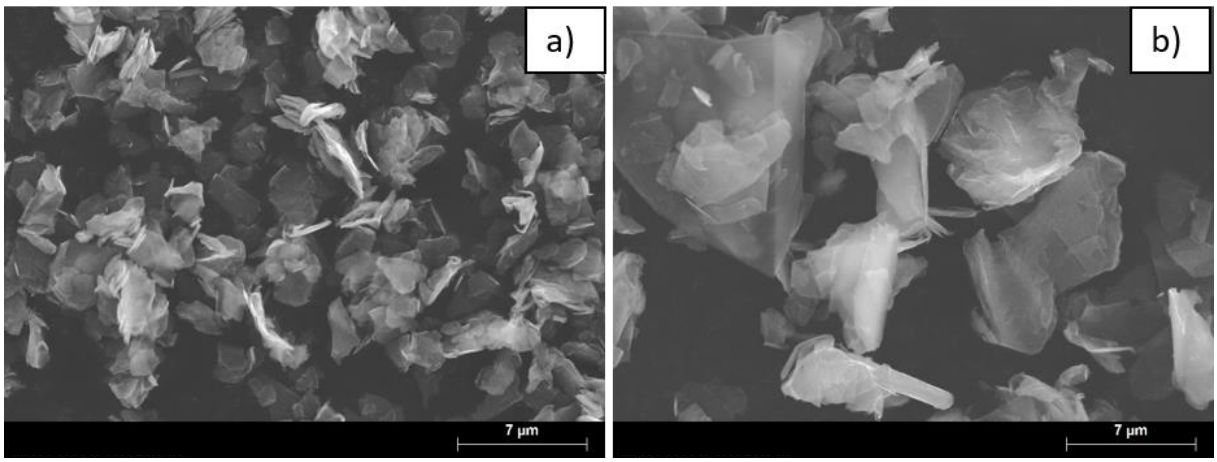

Figure 8 - SEM micrographs of the initial graphite particles. a) - Graphite KS4; b) - Graphite PG10.

The two different types of graphite used are shown on Figure 8, one natural and one synthetic, both supplied by IMERYS. The synthetic graphite (KS4), hereon denominated KS, has a particle size ranging from 2.4 to 4.7 μm, whereas the natural graphite (PM10), hereon denominated PM, has a particle size ranging from 6.4 to 12.5 μm, all guaranteed by the manufacturer.

3.1.2. Weights and Moulds

To compensate capillarity effects during the spheroidization process, thus avoiding particle coalescence, two weights were designed, so that the applied stress on the powder bed would be equal or higher than pressure difference for capillarity effects (ΔP).

The ΔP value for capillarity was calculated by taking the mean particle radius provided by the supplier through equation (9), where γ is the material's surface tension and $r_{particle}$ the particle radius.

Three ΔP values were selected: below, equal and above the value calculated for the mean particle radius. Below the value of ΔP no weight is necessary.

Equation (10), with ΔP input from equation (9), was used to obtain the weights' mass. The material chosen for the weights was stainless steel. With its density, the volume was adapted to both the mould and the required mass. This resulted in two cylindrical stainless-steel weights with 60mm and 30mm in diameter, weighting 1058g and 352g respectively (Figure 9).

$$\Delta P = \frac{2\gamma}{r_{particle}} \tag{9}$$

$$\Delta P = \sigma = \frac{mg}{\pi r^2} \tag{10}$$

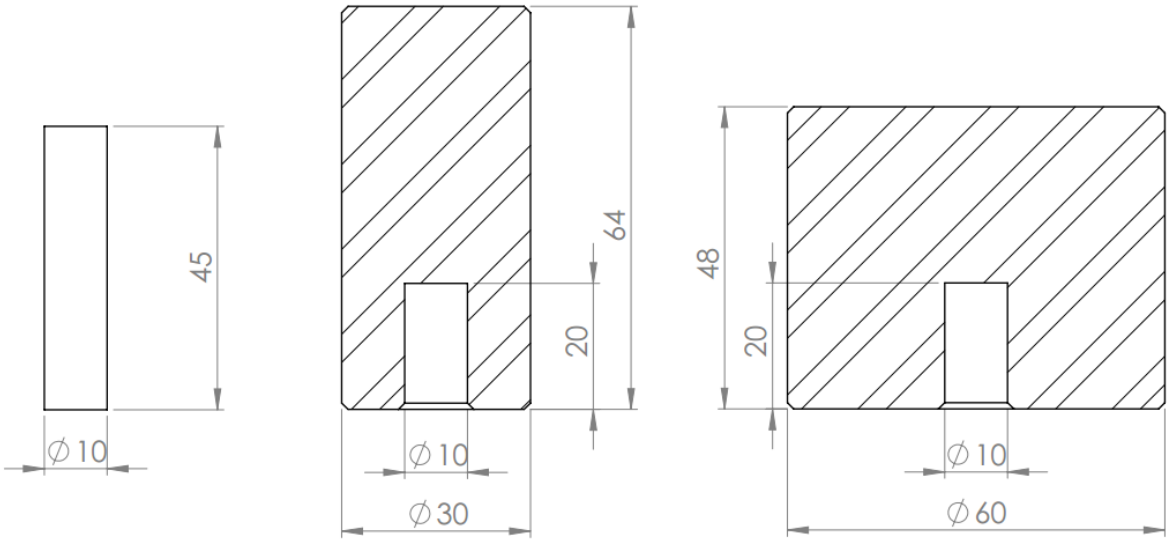

Figure 9 - Technical drawing of the stainless-steel weights and rods used in the spheroidization process.

Table 4 shows the weights dimensions, mass and stress that each one applies on the powder bed.

Table 4 – Dimensions, mass and applied stress for the two designed weights.

Weight	D (mm)	h (mm)	m (g)	ΔP (kPa)
S	30	64	352	44
B	60	48	1058	132

The weights were supported by a stainless steel cylindrical rod of 10mm in diameter and 45mm in length. These components are represented in Figure 9. Both the rod and the weight were machined with tolerances of the order of tens of microns. To prevent contact between the rod and the samples, a graphite rod of 10mm in diameter and 10mm in length was added in between at each end of the cavity, as represented by the technical drawing in Figure 10 of section.

The mould was designed taking into consideration the small amounts of powders under study, as well as the positioning of a weight on top of it. Each mould cavity has variable volume, up to a maximum of approximately 3.5ml.

The mould must remain inert and endure the spheroidization temperature, between 1100 and 1200ºC, without compromising the samples. These conditions, narrowed down the list of possible mould materials to graphite.

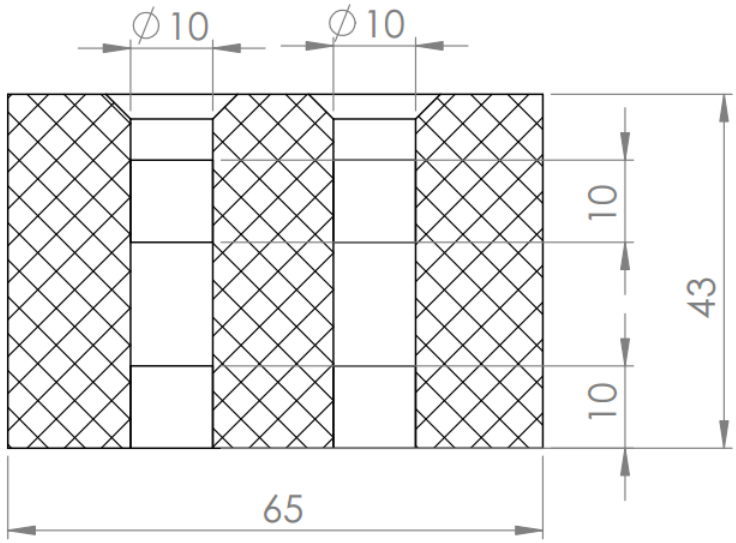

Figure 10 - Technical drawing of the graphite mould, assembled together with the graphite separating rods.

3.1.3. Sample Identification

Copper particles spheroidization was carried out, for both copper-graphite mixes, at 1100ºC and 1200ºC, for 10 and 30 minutes. The applied stress was also a variable under study: S (44 kPa), B (132 kPa) and 0 (for when there was no applied stress).

Samples were identified according to the type of graphite (KS or PG), applied weight (S for small, B for big and 0 for no weight applied), test temperature (1100ºC or 1200ºC), holding time (10 or 30 minutes) and CGR (1:4; 1:2; 1:1; 2:1), in this order.

The combination of all the variables resulted in a total of 32 samples produced. The identification for each sample, within the PG mixture, is explained in Table 5, while that of the KS mixture is done in Table 6.

Table 5 – Copper-Graphite PG10 powder mixture sample identification nomenclature.

			Copper-Graphite Ratio	
T [°C]	t [min]	Weight	1:4	1:2
1100	30	0	PG 0:1100:30:1_4	PG 0:1100:30:1_2
		S	PG S:1100:30:1_4	PG S:1100:30:1_2
		B	PG B:1100:30:1_4	PG B:1100:30:1_2
	10	S	PG S:1100:10:1_4	-
1200	30	0	PG 0:1200:30:1_4	-
		S	PG S:1200:30:1_4	-
	10	0	PG 0:1200:10:1_4	-

Table 6 – Copper-Graphite KS4 powder mixture sample identification nomenclature.

			Copper-Graphite Ratio			
T [°C]	t [min]	Weight	1:4	1:2	1:1	2:1
1100	30	0	KS 0:1100:30:1_4	KS 0:1100:30:1_2	KS S:1100:30:1_1	-
		S	KS S:1100:30:1_4	KS S:1100:30:1_2	KS 0:1100:30:1_1	-
		B	KS B:1100:30:1_4	KS B:1100:30:1_2	KS B:1100:30:1_1	-
	10	S	KS S:1100:10:1_4	-	-	-
1200	30	0	KS 0:1200:30:1_4	KS 0:1200:30:1_2	KS 0:1200:30:1_1	KS 0:1200:30:2_1
		S	KS S:1200:30:1_4	-	-	-
	10	0	KS 0:1200:10:1_4	KS 0:1200:10:1_2	KS 0:1200:10:1_1	KS 0:1200:10:2_1
		S	-	KS S:1200:10:1_2	KS S:1200:10:1_1	KS S:1200:10:2_1

3.2. Particle size distribution

3.2.1. Initial Powders

Analysis of particle size distribution of the original powders, both copper and graphite, was carried out on a Coulter LS230 Particle Size Analyzer, capable of measuring particles with diameters ranging from

0.04 to 2000 µm [43]. This equipment also provides the values of d_{10}, d_{50} and d_{90}, which correspond to the upper limit length for a volume fraction of 10, 50 and 90%, respectively, of the particles.

To compensate for agglomerations occurring on both graphite and copper during the measurements, 3g of a dispersing agent were added to the suspension. The used dispersant was Dolapix.

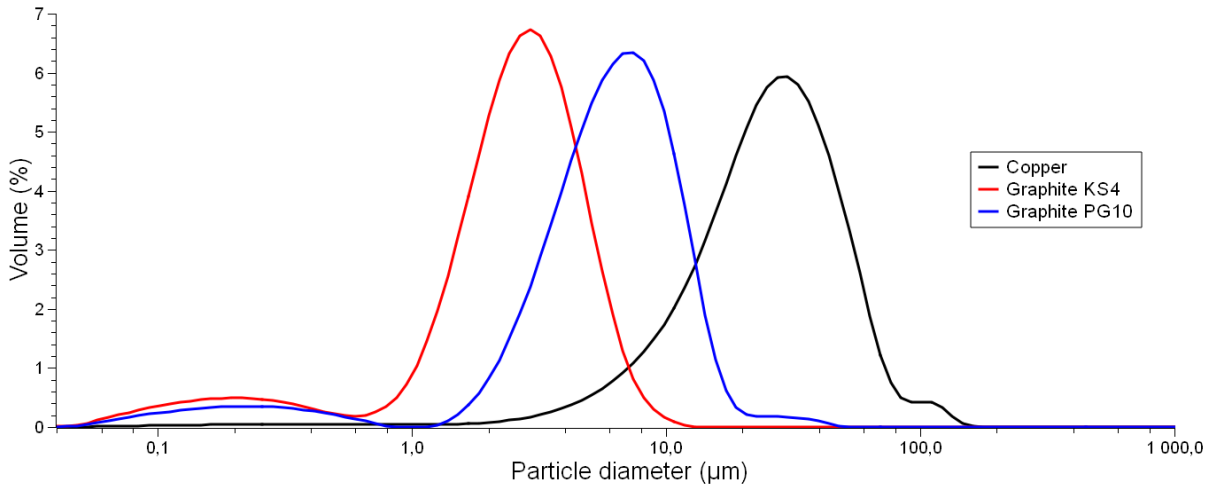

Figure 11 - Differential volume percentage regarding the particle size from the Coulter analysis carried out with the powders: copper, graphite PG10 and graphite KS4, with average diameter values of 31µm, 7µm and 3 µm, respectively.

The results from the size distribution measurement of copper, graphite KS and graphite PM, that are illustrated in Figure 11, show that the particles size reported by the manufacturer is accurate.

3.2.2. Spheroidized powders

To obtain the size distribution of the spheroidized powders diameters, 100 particles were selected among the SEM micrographs taken from each sample that underwent the separation process described later in section 3.3.

The particle size measurement was carried out with the help of an image processing software, ImageJ. All the micrographs were taken with a magnification of 200x in the conditions described in section 3.4.

Particle size was measured by averaging two perpendicular diameters from each particle. To assess the roundness degree of the particles in each sample, a shape factor E_f was applied to all the measured particles, using equation (11).

$$E_f = \frac{d_1}{d_2} \tag{11}$$

3.3. Powder separation

The powder mix was first poured into a vial containing a solution of water-acetone with a proportion of 1:1 in volume. The vial was then sonicated to separate the copper from graphite.

The pre-separated powder mixture was added to the separation media where it stayed for one hour.

The separation media was produced by adding 0,1 ml of hydrochloric acid to 200 ml of distilled water, previously heated to approximately 90ºC. The resulting solution has an acid concentration of 0.006M, which corresponds to a pH of approximately 2.22. The solution was kept at a constant temperature.

After one hour, the graphite was concentrated at the top of the container and the copper powders at the bottom.

Due to the small amount of powder obtained from each of the spheroidization tests, this process was only employed for the mixtures with CGR's of 1:1 and 2:1. In samples with lower fractions, attempts on separating the powders would have resulted in the copper powder being removed along with the graphite.

3.4. SEM and EDS

Scanning electron microscopy (SEM) was used to verify and characterize the powders morphology and to assess their size.

The microscope used, HITACHI S2400, was operated with a voltage of 25 kV and a working distance, WD, of 15 mm. The samples were all loose powders.

The secondary electron, SE, detector was used to acquire topographical images of the samples.

Energy dispersive X-ray spectroscopy analysis (EDS) was carried out to evaluate the specimens' composition, using a Bruker Nano XFlash detector.

4. Experimental results and discussion

In this section, the experimental data from the spheroidization process is presented and analysed, as well as the influence that the separation medium had on particle's morphology.

4.1. Spheroidization process

The starting copper powders' morphology is dendritic, as described in section 3.1.1. The particles mean diameter, measured by the Coulter particle size analyser, was 30.90 ± 20.62 μm, and the values for d_{10}, d_{50} and d_{90} were of 9.59 μm; 26.96 μm and 55.91 μm respectively.

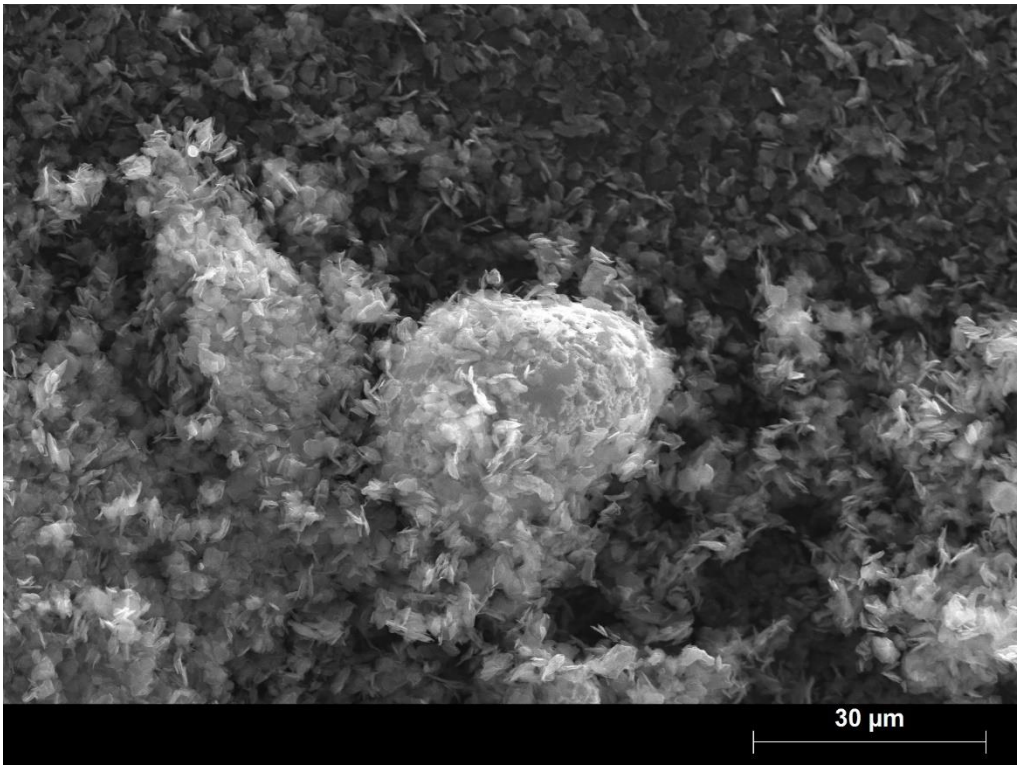

Figure 12 – SEM micrograph of copper particles before the separation process, surrounded by graphite platelets.

The samples underwent a separation procedure, described in section 3.3, to allow for the visualization of the copper particles without the surrounding graphite flakes observed in Figure 12. This separation of copper and graphite powders was only carried out for the batches that with a mass copper-graphite ratio, CGR, of 1:1 and 2:1. In lower proportions, the copper is in such a minute quantity that is washed away in the separation process, therefore, it is not possible to obtain an amount that is representative of the entire sample, which in this work was defined as 100 particles.

The influence of temperature, time, CGR and applied compressive stress on the size and particle's spheroidicity was studied, being represented in terms of diameter and shape factor (equation (11)).

The shape factor provides information on the roundness degree of a set of particles. Since the diameters D1 and D2 are measured perpendicularly, when the shape factor equals one, the particle is considered fully spherical.

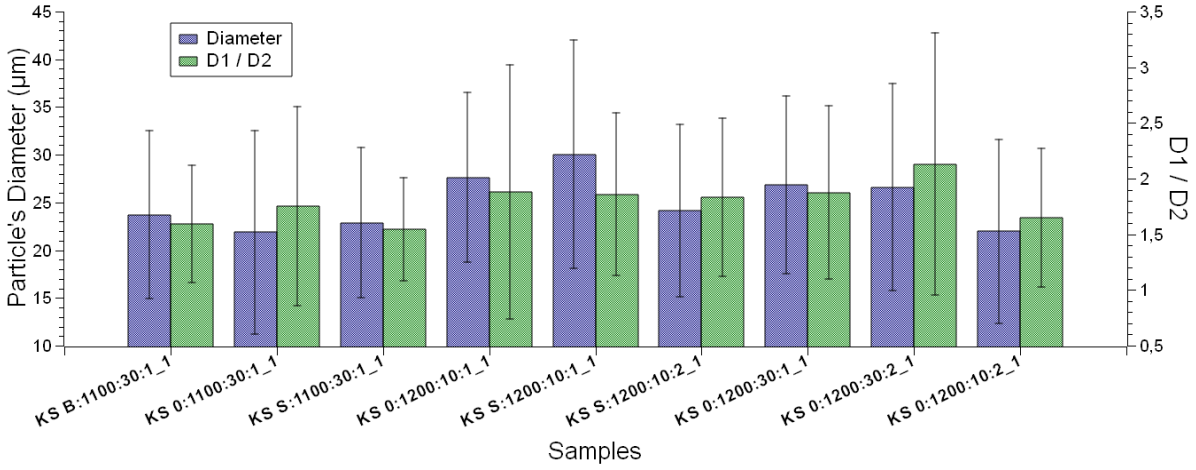

Figure 13 – Samples of individualized particles, with their respective mean diameter (in blue) and their shape factor ratio (in green). The red line represents the mean starting diameter, before the spheroidization process.

In Figure 13 particle's measured diameter is represented in blue and the shape factor d1/d2 is represented in green, with their respective standard deviation. As observed, the standard deviation values are comparable to the average particle diameters. This occurs because the average diameter calculation takes a broad granulometric distribution into a single value. In fact, the initial copper particles diameter was 30.9 ± 19.8 µm. These large standard deviation values are consequently verified throughout all calculations.

The shape factor of all the samples suggests that particles are elongated and not spherical. This is confirmed in Figure 14. Particles tend to be elongated, with one side being 1.5 times the other.

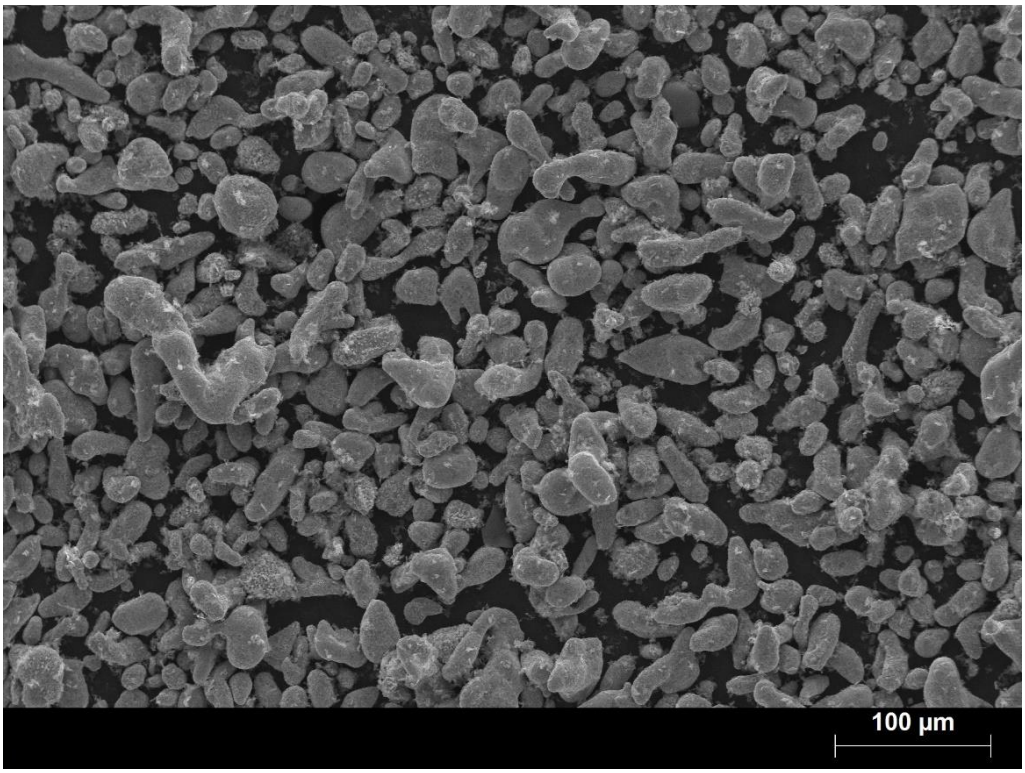

Figure 14 - SEM micrograph of sample KS B:1100:30:1_1 after powder separation. The bigger particles present an elongated shape whereas the smaller ones have more spherical morphologies.

The effect of each of the studied parameters is analysed in detail on the following sections.

4.1.1. Temperature

For the samples treated at the same temperature (KS 0:1100:30:1_1; KS S:1100:30:1_1; KS 0:1200:10:1_1; KS S:1200:10:1_1), it is observed (Figure 15) that a temperature increase of 100ºC led to an increase in particle diameter from 21.88 to 26.84 µm. The shape factor also increased, from 1.75 to 1.87.

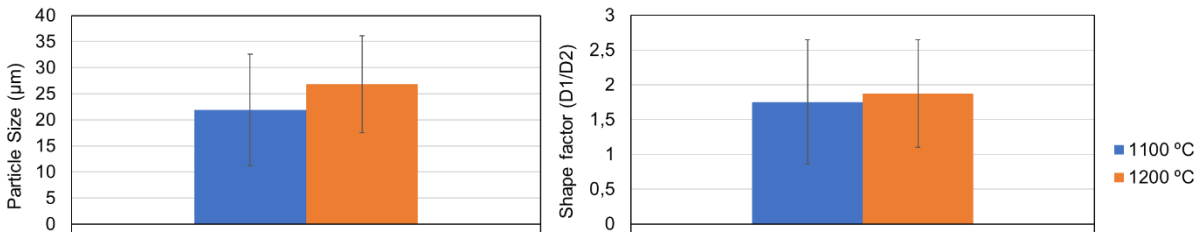

Figure 15 - Temperature influence on the particle's size and shape factor, for a CGR of 1:1, with a 30-minute thermal cycle under no applied compressive stress.

As discussed in section 4.1, the standard deviation values are comparable to the measured particle diameters. Since all values are within error, the temperature influence on particle size and shape factor is not clear.

4.1.2. Copper-graphite ratio

The effect of CGR was studied by comparing particles spheroidized in mixtures with CGR 1:1 and 2:1, at 1200ºC.

For a thermal cycle of 30 minutes and under no applied stress (0), by doubling the copper mass, no alterations were observed (Figure 16).

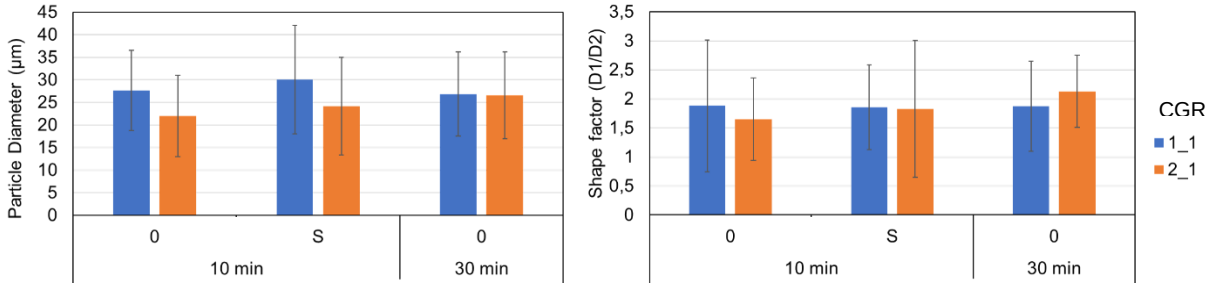

Figure 16 - Influence of the CGR on the spheroidization process of copper particles, regarding particle's size and shape factor. The measured particles were spheroidized at 1200ºC.

By remaining in the furnace for 10 minutes, and for the same weight conditions, the powder diameter decreases from 27.64 to 21.99 µm, accompanied by a decrease in the shape factor, from 1.88 to 1.65.

For the same time interval, but under low stress (S), the particle diameter decreases (from 30.05 to 24.13 µm), when the CGR increases. Regarding the shape factor, no relevant difference was observed.

The desirable result would be a decrease of the particle shape factor, since an elongated particle that is submitted to a temperature above its liquidus temperature, and surrounded by graphite flakes will tend to become spherical to reduce its surface energy, according to equation (3).

4.1.3. Time

These results refer to samples spheroidized at 1200ºC under no applied stress.

For powder mixtures with a 1:1 CGR, the difference between 10 and 30-minute holding time interval is well within the measurement error, for both particle diameter and shape factor (Figure 17).

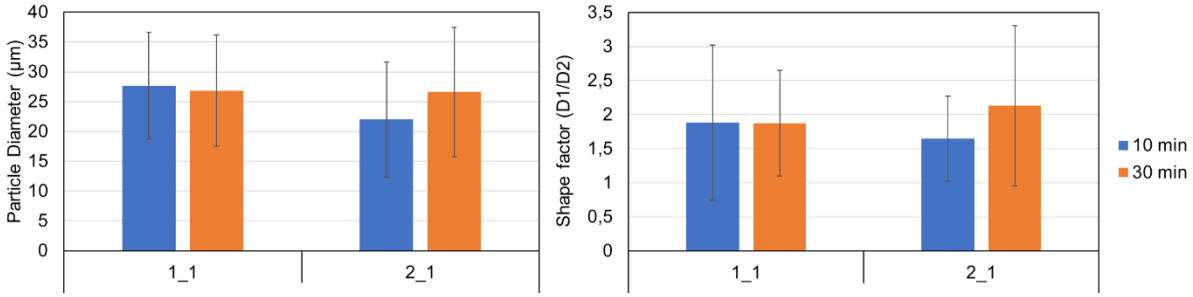

Figure 17 - Time variation from 10 to 30 minutes and its influence on the particle's size and shape factor.

For a 2:1 CGR, the holding time increase resulted in a particle size growth from 21.98 to 26.60 µm, accompanied by an increase of shape factor from 1.65 to 2.13.

Since there is more copper in the mixture, and consequently less graphite, by enduring a longer holding time, copper particles can coalesce due to the proximity between particles. This effect could explain the 21.6% increase in copper particle's size.

4.1.4. Applied Stress

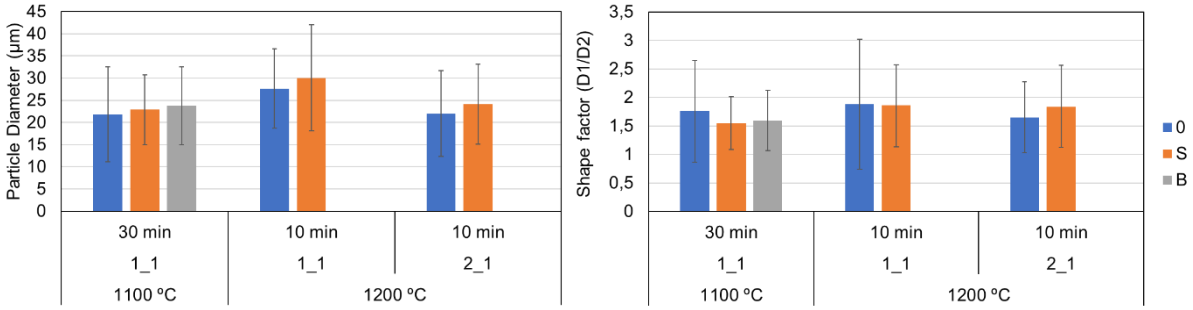

Figure 18 – Applied stress influence on the particle's size and shape factor.

For the 1100ºC, 30-minute sample, as indicated in Figure 18, it is observed that a gradual particle size increase from 21.88 to 23.71 µm. Regarding the shape factor, it was lower for the smaller weight (S), with 1.54, and higher when no weight was applied, 1.75.

For the 1200ºC, 10 minute samples, an increase on the applied weight also translated into an increase on the particle's size, from 27.64 µm to 30.05 µm and from 21.96 µm to 24.13 µm, for both CGR 1:1 and 2:2, respectively. However, when considering the shape factor, a slight decrease is observed on the samples with a 1:1 ratio (1.88 to 1.86), and an increase on the 2:1 ratio samples (1.76 to 1.84).

Once again, the standard deviation values do not allow a correct evaluation of the influence of applied stress on powder spheroidization.

4.1.5. Powder contamination

Copper powders are submitted to multiple processing steps, therefore, it is important to assess their surface contamination, with special attention to oxygen, since these were initially low-oxygen copper powders.

Figure 19 shows the EDS spectrum of copper powder's surface before any procedure, after the spheroidization process and after the separation process. One EDS spectra of each is represented in Figure 19-d).

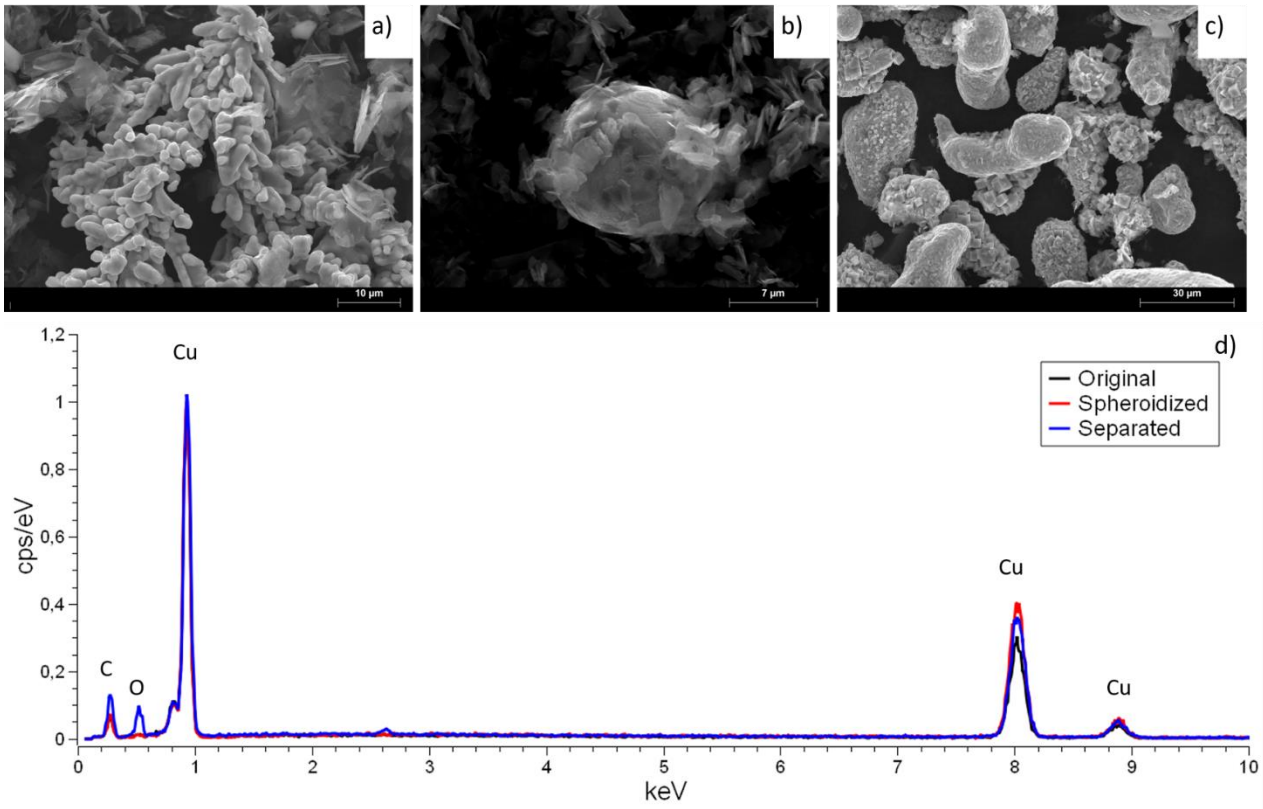

Figure 19 – Micrographs of the particles used for the EDS analysis: a) Original copper powders; b) Copper powder after spheroidization process; c) Powders after separation process. d) Normalized EDS spectrum of the different step samples: original powders (black line), powders after spheroidization (red line) and powders after the separation process (blue line).

The characteristic X-ray values of copper (Kα – 8.046 keV, Kβ – 8.904 keV, Lα – 0.928 keV, Lβ – 0.947 keV) are present on all spectra. Few to no oxygen is observed at the surface on the original and spheroidized samples, appearing only in the sample that underwent the copper-graphite separation process. This suggests copper powder surface oxidation.

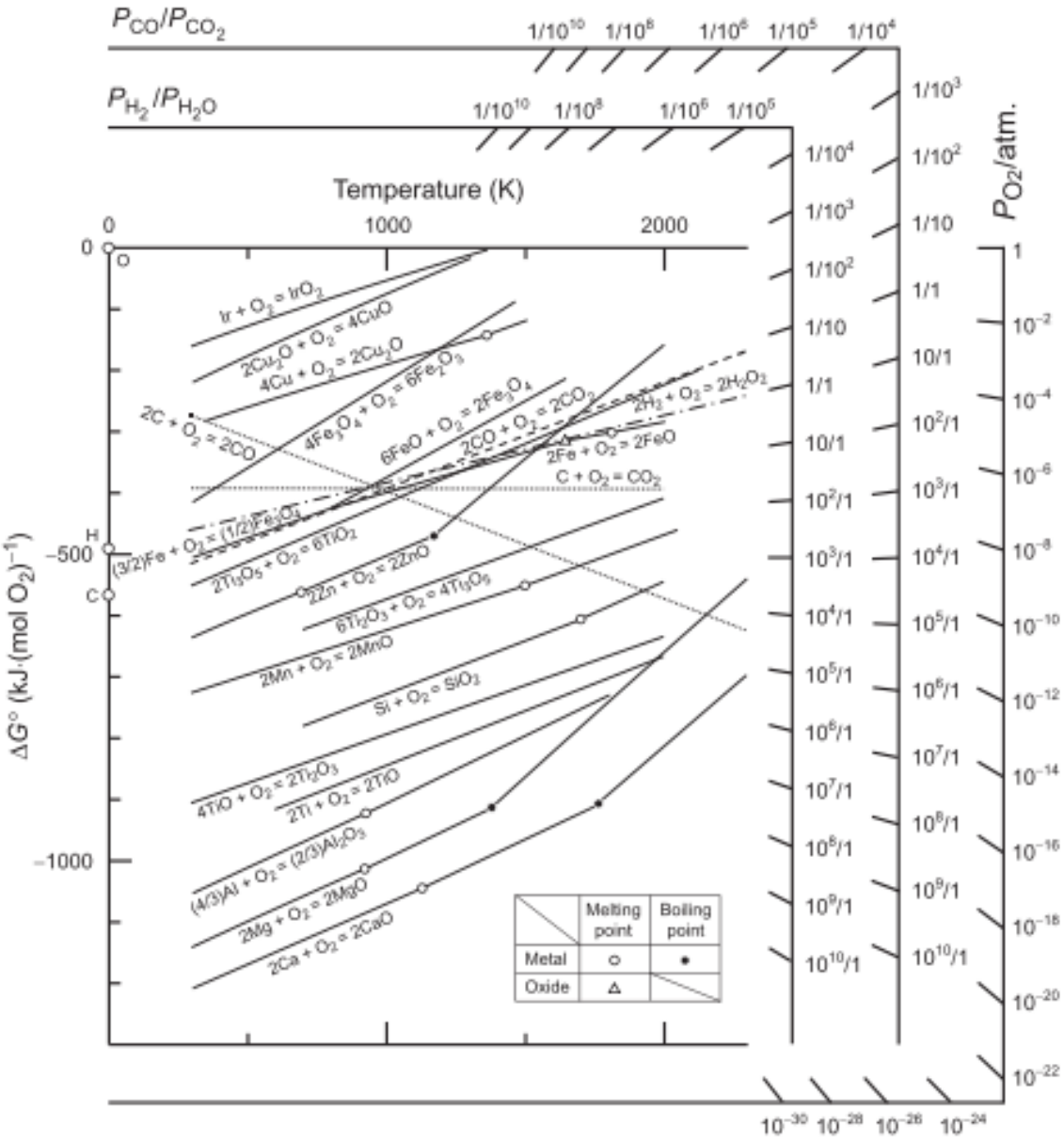

Figure 20 – The Ellingham diagram [44]**.**

The Gibbs free energy (ΔG) of a reaction is a measure of the thermodynamic driving force that makes a reaction occur. A negative value for ΔG indicates that a reaction can proceed spontaneously without external inputs [44]. The Ellingham diagram (Figure 20) shows a plot of ΔG^o with temperature, for metals reacting with oxides.

Spheroidized particles maintain an oxygen content similar to the original copper powders. This was expected for two reasons: the process was carried out under vacuum and the oxygen reduction reaction to carbon monoxide has a lower ΔG^o than the formation of any copper oxide, as observed in Figure 20, hence removing any oxygen amount that the vacuum system could not remove.

4.2. Influence of the separation medium on the particle's morphology

As described in section 3.3, the separation between copper and graphite particles was carried out in an aqueous solution of hydrochloric acid with a concentration of 0.006 M. This proved to be an effective copper extractor as referenced in the literature [45].

For a low concentration of hydrochloric acid such as 0.006 M, the pH is approximately 2.22. As expected, such a low pH has a considerable influence on the particle's final morphology, as observed in Figure 21. This occurrence was verified on all the samples that underwent the separation procedure.

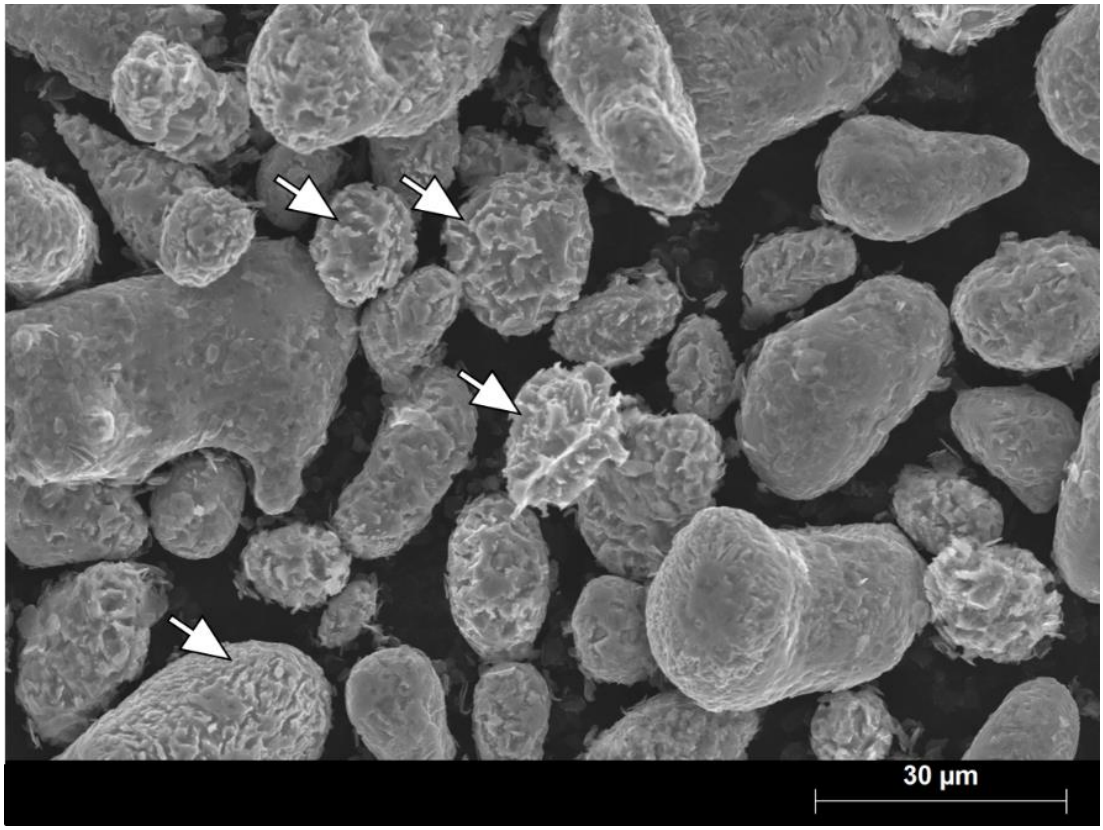

Figure 21 - SEM micrograph of sample KS 0:1200:10:2_1 after the separation process with some severely corroded particles identified with arrows.

Some of the particles presented in Figure 21 appear to be corroded on the surface. This could be explained by the corrosion behaviour of copper in oxygenated hydrochloric acid solutions. This effect seems more preponderant in smaller particles than in bigger ones.

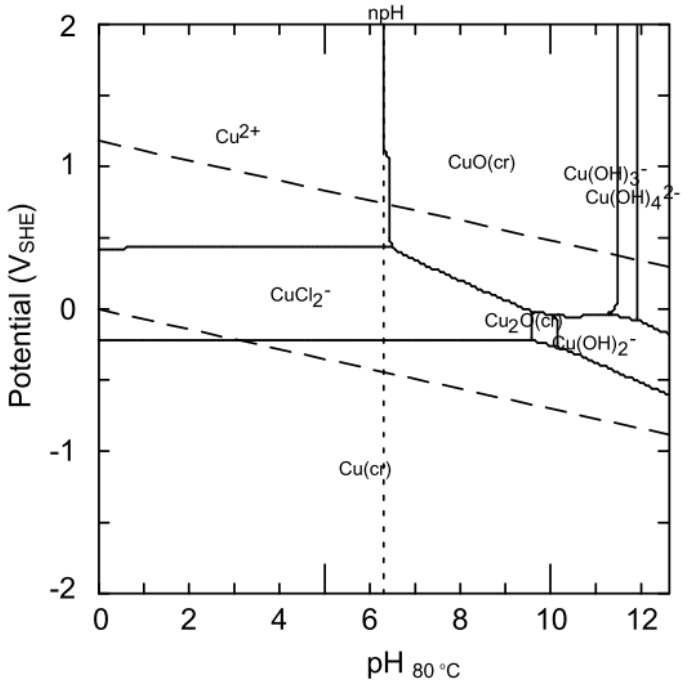

Figure 22 - Pourbaix diagram for copper in the copper-chlorine-water system at 80ºC [46]**.**

Copper anodic dissolution is influenced by the chloride concentration. In fact, copper dissolution, which at low chloride concentrations occurs through the formation of CuCl, increases linearly with time [47]. Copper cations go to the solution and when these react with chloride ions, cuprous chloride (CuCl) is formed on the powder's surface. The latter does not provide enough protection because since it transforms into the soluble copper chloride complex, $CuCl_2^-$ [46][47]. This complex will decrease the immunity of the passivated areas on the copper powder's surface thus increasing the weight loss effect of the particle by copper corrosion. This is illustrated in the Pourbaix diagram of copper (Figure 22) in a copper-chlorine-water system at 80ºC [46], 10ºC below the used separation temperature.

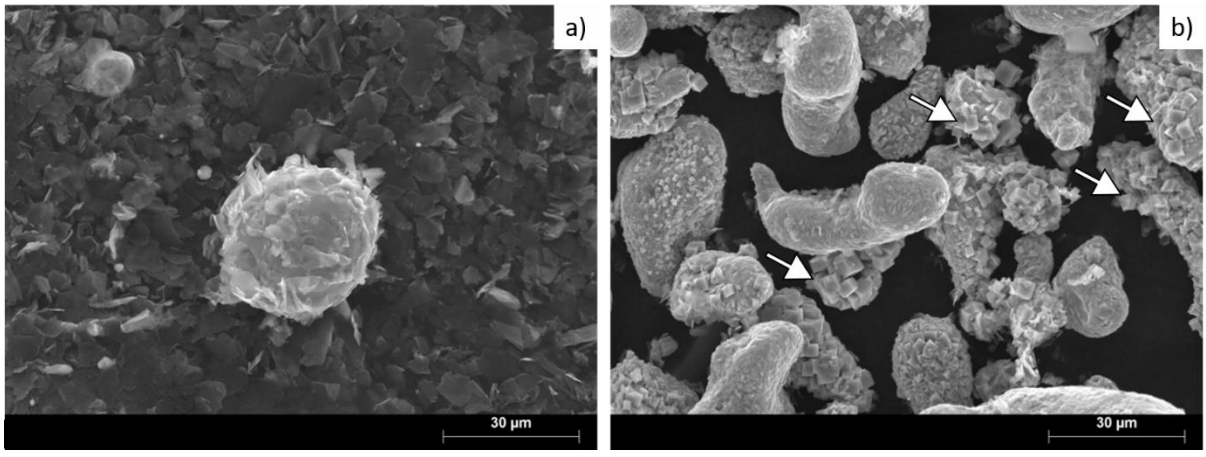

Figure 23 - Copper particle's morphology comparison after the separation process in an 0.006M hydrochloric acid aqueous solution. a) particle before separation procedure; b) particles after separation, where corrosion effects are visible (identified with arrows).

Figure 23 shows a comparison between particles before and after being submitted to the separation process. On Figure 23 it is possible to observe copper cubes on the surface of small size particles. This effect is not present on all samples. Further work on this topic could unveil the cause of this occurrence.

4.3. Summary

Copper particles were submitted to a spheroidization process on a graphite powder bed, under different processing parameters. Alterations on the previously dendritic particles were observed. Since graphite platelets remained on the copper particle surface, it was necessary to separate copper from graphite. A hydrochloric acid solution was used as separation medium, under 90ºC for 1h. After the separation process, all the samples were observed on the SEM, and 100 particles per sample were measured.

The particle shape of all the observed samples (CGR of 1:1 and 2:1) changed after the spheroidization process. Table 7 presents a summary of the particle's measured diameter and shape factor. Due to a high standard deviation, it is not possible to conclude the influence of each parameter on the spheroidization process.

Table 7 - Particle size diameter and spheroidicity ratio for the cleansed particles, and their respective processing parameters.

Sample	Temperature	Time	CGR	Applied Stress	D1 / D2	D
KS B:1100:30:1_1	1100	30	1:1	B	1.60 ± 0.53	23.71 ± 8.78
KS 0:1100:30:1_1	1100	30	1:1	0	1.76 ± 0.89	21.88 ± 10.69
KS S:1100:30:1_1	1100	30	1:1	S	1.55 ± 0.46	22.86 ± 7.85
KS 0:1200:10:1_1	1200	10	1:1	S	1.88 ± 1.14	27.64 ± 8.93
KS S:1200:10:1_1	1200	10	1:1	S	1.86 ± 0.73	30.05 ± 11.98
KS S:1200:10:2_1	1200	10	2:1	S	1.83 ± 0.71	24.13 ± 9.02
KS 0:1200:30:1_1	1200	30	1:1	0	1.87 ± 0.78	26.84 ± 9.30
KS 0:1200:30:2_1	1200	30	2:1	0	2.13 ± 1.18	26.60 ± 10.83
KS 0:1200:10:2_1	1200	10	2:1	0	1.65 ± 0.62	21.99 ± 9.65

The graphite-copper separation process is effective but induces changes in the previously spheroidized particles. After the separation procedure, some samples exhibited particles with cubes on their surfaces. No similar results were found in literature, thus further word on this topic is suggested to understand this occurrence.

Since the primary purpose of this work's section was to spheroidize the copper particles, any morphology modification after this process is not desirable, hence an alternative separation method should be studied.

5. Modelling

FEM simulation of hardness tests on porous bodies could help validate constitutive equations for plastic deformation of porous solids.

A material model that enables the manipulation of porosity percentage will be used to simulate porosity in copper bodies. This model will be matched against known material models, such as the Johnson-Cook model of plasticity. Simulations will be carried out to test the influence of indenter size and porosity on the BHN.

The Modelling section comprises the creation of the model under study, the identification of relevant variables, and the tests carried out along with results from the simulations.

5.1. The Model

FEM simulations could be used to assess a material's porosity by conducting a hardness test without having to resort to complex tests. For now, this model aims to be the first development in this sort of studies.

The Brinell hardness test was chosen due to the indenter geometrical shape. Sharp edges could be interpreted as singularities resulting in problems such as lack of convergence. The use of a round indenter allows to avoid such problems.

The model itself must be a very close replication of the hardness test i.e., indentation of the sample surface along the vertical axis; hold the indenter in place for the standard period, indenter removal and hardness measurement.

In the following subsection, the steps taken for the model creation as implemention in Abaqus are described.

5.1.1. Parts

The ideal finite element model for the simulation of the hardness test on sample with controlled porosity would be a three-dimensional representation of the problem. This would better represent the random distribution of voids inside the material under study as well as the stress flow throughout the test piece. However, to reduce computation time, hence allowing for more simulations and more variability conditions within the model under study, some simplifications are proposed.

The first simplification was to reduce the 3D model to a 2D axisymmetric one, allowing for a sharp decrease in element number and computation time. If the voids were included as geometrical holes, it would not be possible to create an accurate 2D axisymmetric model, since the voids would become toroidal holes throughout the sample, after the solid revolution, and not as discrete spherical ones. The voids were therefore included as corrections in the material properties and not as geometrical entities.

The fact that the load is applied along the vertical axis with the stress flow being equally distributed in the perpendicular directions sustains the choice for an axisymmetric model.

In the following subsections, the development of the different model components is explained in detail.

- Ball indenter

In Brinell hardness testing, the indenter is a tungsten carbide (WC) sphere [32].

The ball indenter can have three possible diameters: 2.5; 5 and 10 mm [31]. Because the model is created with a 2D axisymmetric configuration, the indenter is represented by a semi-circle (Figure 24 a)). The indenter's material has a Young modulus several times higher than that of copper. For this reason, the indenter will only experience elastic deformation, and even this value will be small enough to be neglected. Therefore, and since the purpose of this work is only the study of the behaviour of the copper body, the indenter was defined as a rigid solid.

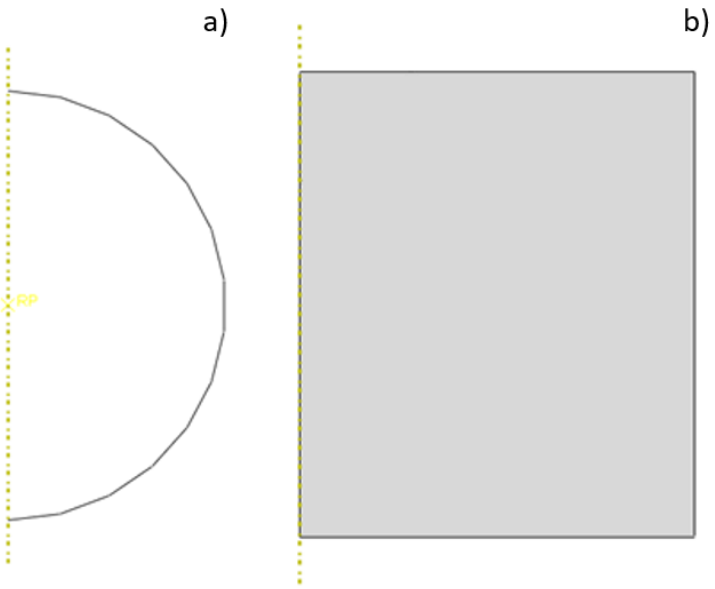

Figure 24 – Representation of the model's parts: a) Indenter sphere defined as a rigid material; b) Copper body, defined as elasto-plastic material.

- Body

The copper body (Figure 24-b)) on which the indentation will be carried out was created with 42 mm in height by 35 mm in width, with both values being more than five times the indenter radius. This was done to prevent any boundary effect propagation onto the indentation region.

Unlike the indenter, the body will be subjected to both elastic and plastic deformations.

5.1.2. Materials

For the computational model, and since any deformation on the indenter is neglected, it is not necessary to assign material properties to it, within the model.

The material under study is electrolytic copper. Since the aim of this project is to study porous materials, it is necessary to cast aside the classical plasticity models. The chosen model is based on the Gurson-Tvergaard-Needleman model. It allows to freely change the relative density of the material, between 1 and 0.9, thus controlling the porosity content from 0% to 10%. When porosity is set to 0%, the model represents a fully dense body, allowing for comparison with other standard models for dense materials. For this purpose, two different models were created, one that represents the desired porosity (GTN) and another fully dense material (CPM). Their specifications are described in detail in the following two subsections.

- Fully dense material

There are several dense material models available in the literature. The one chosen for this comparison, the Johnson-Cook plasticity model [48] (equation (12)) takes as input the material parameters found in Table 8, with σ being the equivalent stress, ε_p the equivalent plastic strain, $\dot{\varepsilon}$ the strain rate, $\dot{\varepsilon}_0$ the normalizing strain rate and *A*, *B*, *C* and *n* the empirical model parameters.

$$\sigma\left(\varepsilon_p, \dot{\varepsilon}\right) = \left(A + B{\varepsilon_p}^n\right)\left(1 + Cln\frac{\dot{\varepsilon}}{\dot{\varepsilon}_0}\right) \tag{12}$$

The material properties introduced in Abaqus are part of the Johnson-Cook model of plasticity, with no consideration for temperature influence. Table 8 summarizes the chosen parameters and the sources from which they were obtained.

Table 8 - Johnson Cook material's properties and parameters introduced for the tensile test simulation [49]**.**

Material Properties	Value	Units	Reference
Density	8950	Kg/m³	[50]
Young's Modulus	125	GPa	
Poisson's ratio	0.35	-	
A	90	MPa	[51]
B	292	MPa	
C	0.029	-	
n	0.31	-	
$\dot{\varepsilon}_0$	1	-	
D_1	0.54	-	[48]
D_2	4.89	-	
D_3	-3.03	-	
D_4	0.014	-	

- Porous material

The porous material was defined according to the GTN model described in section 2.4.3.

The GTN model only presents reliable data for relative density higher than 0.9, which implies a maximum porosity of 10% [52], [53]. Compaction studies carried out on copper powders show that a pressure above 300 MPa produces relative densities well above 0.9 [54]. These powders would have to be compacted at an assumed pressure above 300 MPa and sintered to be usable.

Table 9 - Materials parameters and properties for the GTN porosity model to be introduced in Abaqus.

Material Properties	Value	Units	Reference
Density	8950	Kg/m³	[50]

Young's Modulus	125	GPa	
Poisson's ratio	0.35	-	
Yield stress	-	MPa	-
q1	1.5	-	[42],[55]
q2	1	-	
q3	2.25	-	
Friction coefficient	0.75	-	[56]

Both material models require data from stress-strain curves and therefore, in this modelling project, a tensile test was created to provide the necessary input to the material models.

The specimen was created according to ASTM E8/E8M – 09 [57] and meshed with 15780 C3D8R elements, and 20016 nodes, as illustrated in Figure 25.

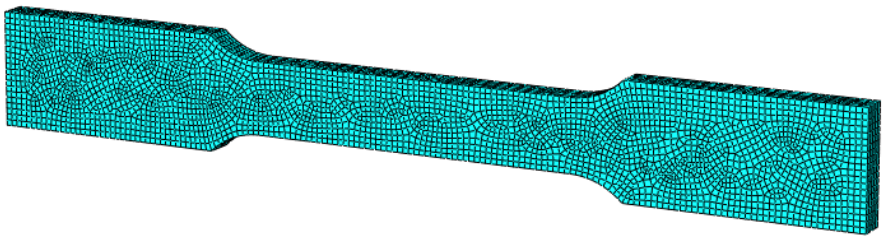

Figure 25 - Meshed tensile test specimen, with 15780 C3D8R elements, 20016 nodes, and rectangular cross-section.

One side of the specimen was *encastred* and the other end was subjected to the tensile movement.

The same standard requirements were used for the tensile test procedures, namely the testing speed, which was set to 0.5 mm per minute.

5.1.3. Assembly

The assembly of the indenter and sample parts is carried out according to the desired position for the start of the test. Figure 26 illustrates the relative positions of the indenter and the sample body.

In hardness testing the indenter is not initially in contact with the sample. This only happens after the test is in motion. However, to save computational time, the indenter was set to start the simulation in contact with the body. This choice of assembly also facilitates the creation of contact properties.

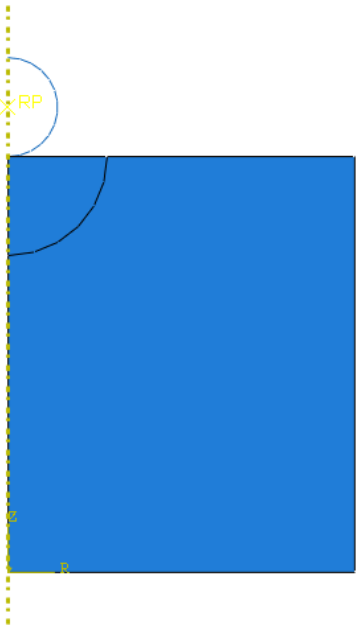

Figure 26 - Assembly of all the components on their starting positions on the hardness test.

5.1.4. Step

The mechanisms set to occur during the simulation are created in the step section based on the type of process under study.

For this specific situation, given that the model is defined by a low deformation rate of the body and small displacements from the indenter, the step was defined as *static general*, with the specifications presented in Table 10. The same values were used in the final simulations.

Table 10 - Step incrementation parameters introduced in the software.

Time period	Maximum number of increments	Increment size		
		Initial	Minimum	Maximum
12	650	0.0001	0.000011	1

Two steps were created in the model. The first step, *Indentation*, simulates the indentation process itself, accounting for the specimen penetration and holding time, defined by the standard applied throughout the whole model [31].

The second step, *Removal*, refers to the removal of the indenter from the sample. This step was defined with a normalized time interval of 1. Apart from this, all other parameters are as described in Table 10.

5.1.5. Interaction Properties and Contact

As stated before, contact is made between a rigid and a deformable material, the indenter and the copper body respectively. For this purpose, *surface-to-surface* contact interaction was chosen as the type of contact to be applied to the model from the initial step stage to the end. The selected surfaces are illustrated in Figure 27. The rigid surface was chosen as the *first* or *master* surface (in red) and the deformable surface was chosen as the *second* or *slave* surface (in purple). In terms of sliding formulation, *Finite sliding* was chosen due to its broader formulation. It allows any arbitrary motion of the surfaces [53]. This eases the convergence during the simulation.

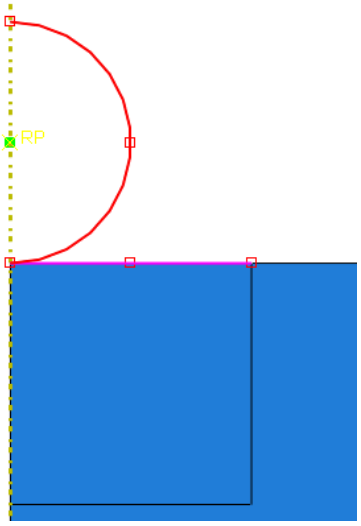

Figure 27 - Selected surfaces on which the contact properties are applied. In red in the *master* surface (indenter's surface) and in purple is the *slave* surface (sample partition's surface).

The contact conditions dictate how the surfaces will act based on the properties selected for the interaction itself. Regarding this matter, two different behaviours were selected: *normal behaviour* and *tangential behaviour*. The friction coefficient is introduced in the model as part of tangential motion.

These parameters were the same for all simulations.

5.1.6. Boundary Conditions and Load

Boundary Conditions (BC) were defined for both the indenter and the body.

For the body, BC's were set on two different edges. On the lateral vertical left edge, the BC was created to ensure symmetry along the r-axis, so that no deformed material flows to the symmetry axis of the

model. On the bottom edge, the BC was set as *encastre* to prevent any movement once the indentation process begins.

For the indenter, it was necessary to create a movement restriction, allowing only for displacement along the vertical y-axis.

Figure 28 shows the boundary conditions applied to the computational model.

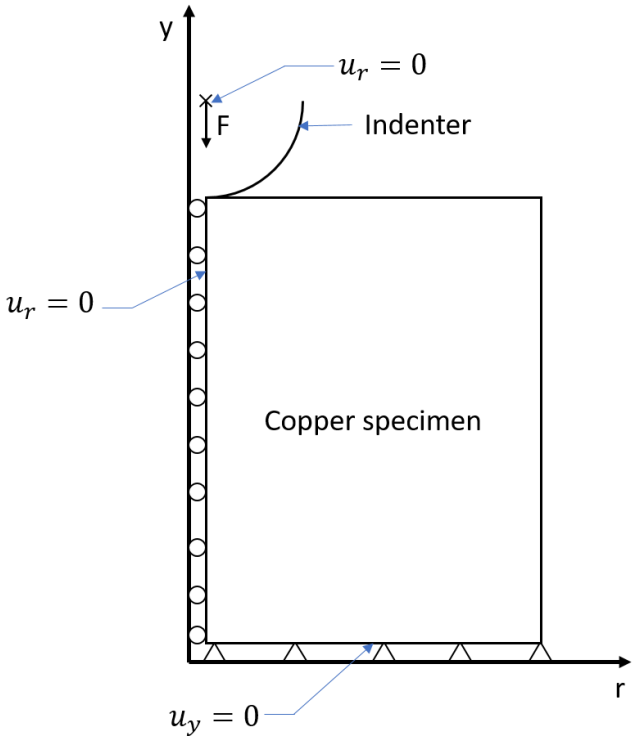

Figure 28 - Schematics of the boundary conditions applied to the hardness model.

A compressive load was created on the reference point of the indenter. Table 11 presents the possible load intensities allowed by the standard [31] for each ball diameter used during the mesh study and final simulations.

Table 11 - Ball diameter, test load and force-diameter ratio used in the simulations [31]**.**

Ball Diameter [mm]	Test load		F/D² ratio [kgf/mm²]
	N	kgf	
10	14710	1500	15
10	9807	1000	10
10	4903	500	5
5	2452	250	10
5	1226	125	5
2.5	612.9	62.5	10
2.5	306.5	31.25	5

5.1.7. Mesh

To calculate the material functions addressed in the previous sections, the software needs the location of nodes and elements provided by the mesh, so it is mandatory to mesh each of the model's parts. Choosing the correct mesh requires balance and sensitivity to the condition under study. Too coarse and the model will be faster when simulating but will stray from the reality; too fine of a mesh could provide results very close to reality, at the expense of simulating time, since the software must solve a very high number of equations. By running several trial-runs, it is possible to choose the conditions that best simulate reality without taking too long to obtain them.

The trial simulation methodologies were applied in this process to access the ideal parameters for the hardness test, in terms of partition's shape, mesh size and type of elements.

- Indenter

The indenter was defined as a rigid part, but still requires a mesh. Since there is no deformation occurring on the indenter, the mesh considerations are not as important as in the body. Therefore, only one parameter was taken into consideration: the section of the indenter that was close to the contact region between the parts had to be more finely meshed than the section that was not involved in any contact mechanism, so that more indenter's nodes are in contact with the body. The indenter was meshed with 41 nodes and 40 elements.

- Body

Unlike the indenter, the Body will undergo plastic deformation during the hardness test. During a finite element method simulation, plastic yield and strain propagation are influenced by the mesh, geometry and size.

On Brinell hardness test, the hardness number is calculated with equation (4), by providing the radius of the indent left by the probe. From the simulation results, the radius is taken as the distance from the symmetry axis to the node that remains in the original position (Figure 29), and so it is highly influenced by the meshing of the part.

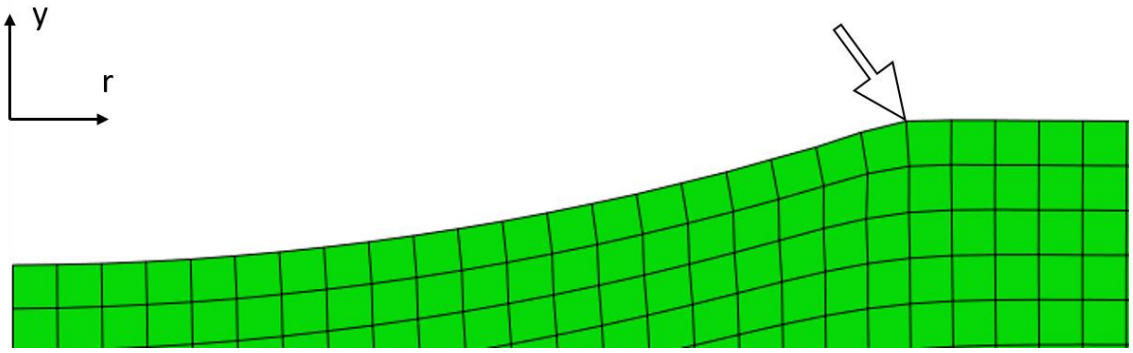

Figure 29 – Identification of the node that is used to assess the indentation radius.

Consequently, it becomes relevant and necessary to perform a thorough study on this parameter to assess the mesh that better correlates to experimental hardness.

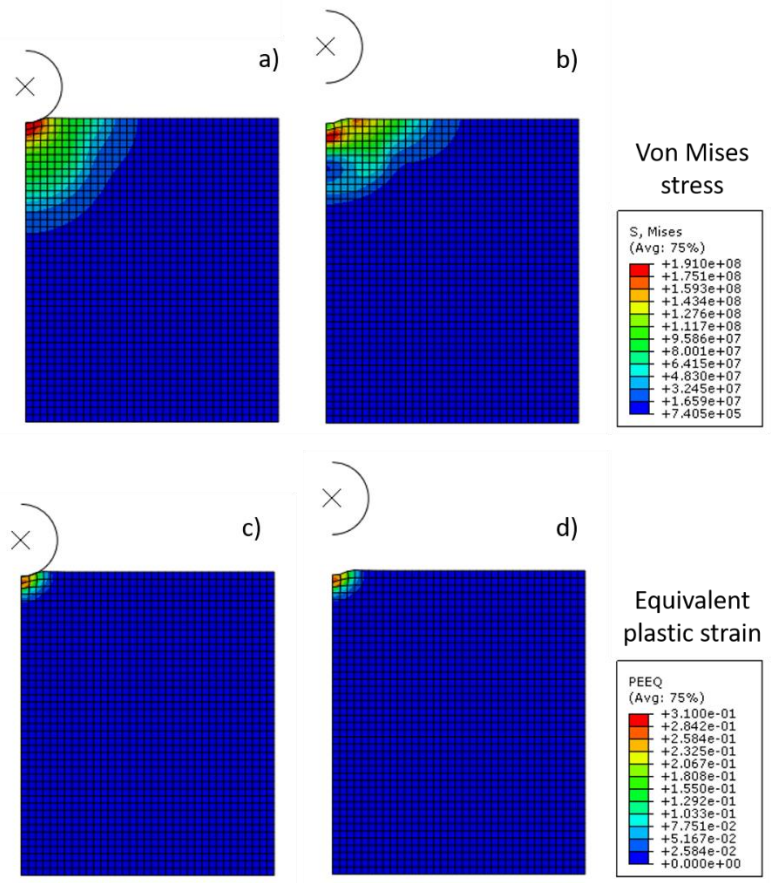

Figure 30 - Mesh study baseline results, displaying the Von Mises stress for the indentation a) and removal b) steps, as well as the equivalent plastic strain, c) and d), for the same simulation steps.

An advantage of only having one deformable body is that the mesh study can be carried out as a trial and error approach without having major implications on the remaining parts of the model.

An automatic mesh was automatically generated by the software on the part's domain with quadrangular elements. Even though it created a very coarse mesh, it serves as an example to observe the stress and plastic deformation across the body (Figure 30), as well as the indentation and removal mechanism. The model debugging also occurred during this stage.

It was possible to observe that stress propagated only to the region below the indenter. This justifies the reduction of the number of elements spread throughout the sample concentrating them in the indentation region. For this purpose, a partition with a length of 10mm was created. This size was chosen to ensure that all the plastic deformation remains inside the partition.

As described earlier in this section, any modifications to the elements, or mesh, may have a big impact on the final hardness results. Therefore, the partition's shape will also constrain the number of elements

and their respective distribution. To test the magnitude of this effect, two partition configurations were tested: a circular partition and a square partition.

The body mesh can be composed of triangular or quadrangular elements, or a combination of both. Quadrangular elements can adapt more easily to deformation, since they have more faces and vertices to move and accommodate deformation, than triangles. On the other hand, triangular elements have a better fitting to the partition's shape than quadrangular elements. It is therefore necessary to analyse the influence of each element on the overall simulation.

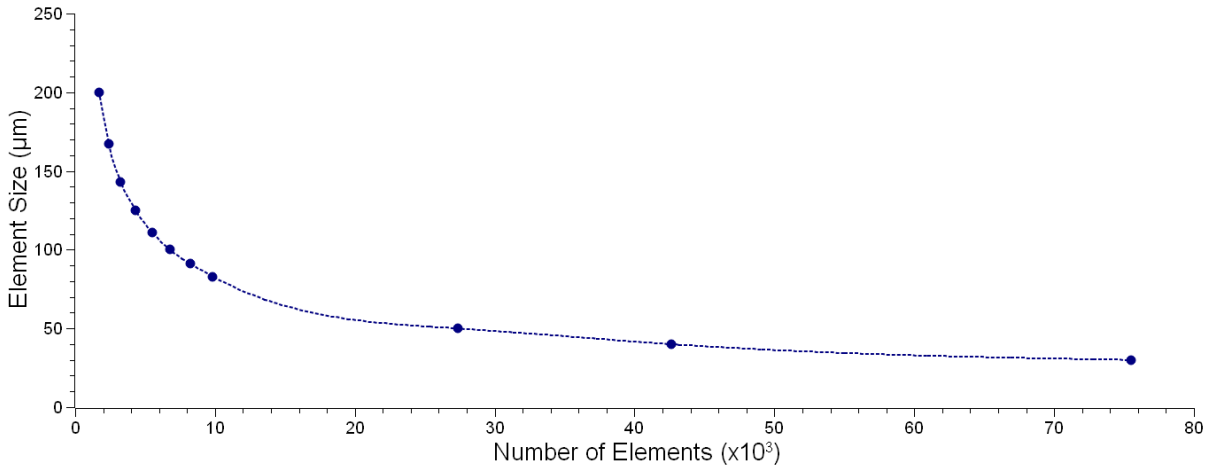

Figure 31 - Elements size variation with the number of elements present in the partitioned region of the deformable body.

When triangular elements were chosen, the software automatically generated a mesh, since these elements are more versatile than quadrangular elements. However, with the latter it was not possible to generate a mesh due to the high distortion of the elements. To correct this, the outer elements were defined as triangular elements.

To identify the number of elements necessary to the model, the partition was *seeded*. Seeding is the operation of defining the number or size of divisions required per edge of the body to be meshed. An element size evaluation was made by ranging element's dimensions from 20 to 200 µm. By decreasing the element's size, one increases their number. This relationship is illustrated in Figure 31.

Two partition configurations and two different elements result in 4 attempted test conditions for each of the element's size, as represented in Figure 32, representing a total of 44 simulations carried out to study the mesh.

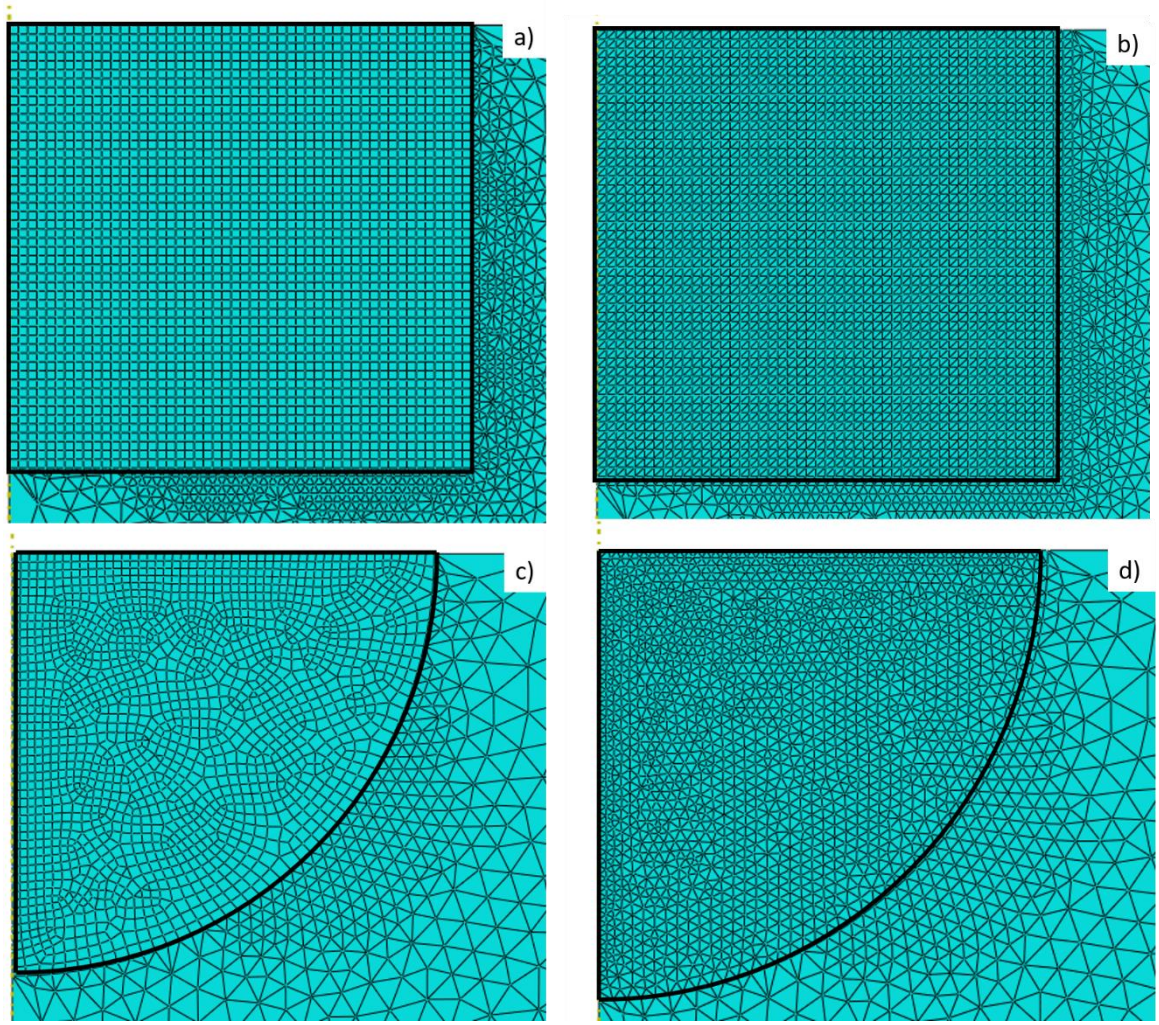

Figure 32 - Different configurations for the tested parameters of partition shape and element's geometry: a) square partition with quadrangular elements; b) square partition with triangular elements; c) circular partition with quadrangular elements; d) circular partition with triangular elements.

Given that the purpose of this initial study is to evaluate the mesh according to the multiple parameters above mentioned, the load and the indenter's diameter were kept constant at 1500 kgf (14710 N) and 10 mm, respectively. Test results are shown in Figure 33 to Figure 37.

The stress curves from Figure 33 represent the maximum value of Von Mises stress at the minimum vertical indenter position (at the end of the indentation step) (full line with dot markers) and at the end of the removal step (maximum residual stress) increment (dashed line with cross marker) as a function of the number of elements. For the four test conditions, it is possible to denote differences between quadrangular and triangular elements. Even with different partition shapes, all simulations using quadrangular elements show some consistency, while those using triangular elements present significant changes between the circular and the square partitions.

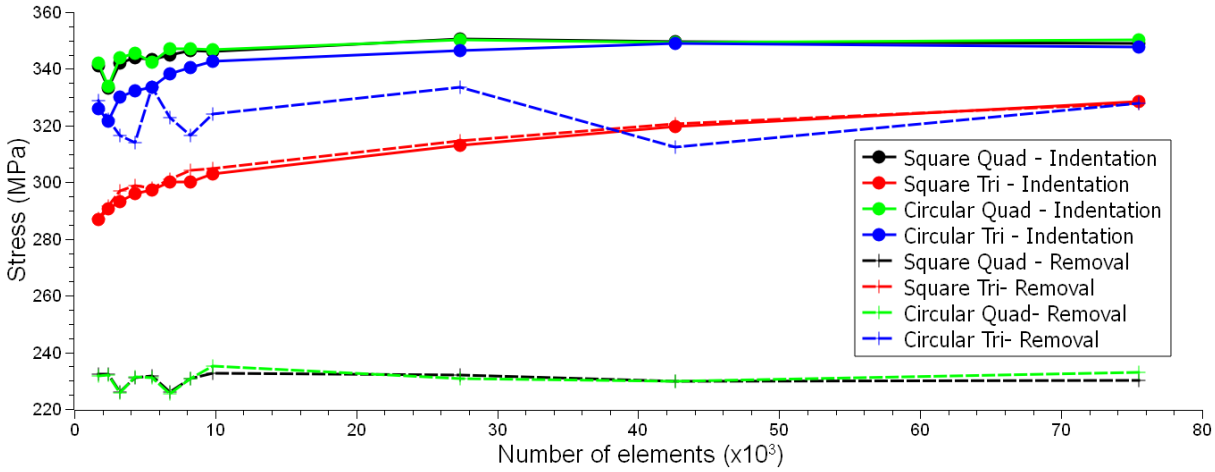

Figure 33 - Maximum values of Von Mises stress at the end of the indentation and removal steps plotted against the number of elements of the body.

After undergoing plastic deformation, the material recovers its elastic deformation [58]. Therefore, the removal step plot is expected to be placed below the indentation step plot. This is verified for all tested conditions, except for the model with a square partition and triangular elements (Figure 33). For the others, quadrangular elements have a higher difference between the indentation and removal steps for maximum stress produced by the simulation.

Figure 34 represents the stress curve variation and its derivative. The derivative provides information on the stability of the model with increasing number of elements: the derivative will tend to zero in models with higher stability. Triangular elements show an ever-changing plot of the stress curve. The circular partition with triangular elements (Figure 34 - d) eventually reaches a plateau, but for more than 40000 elements. Steady stress values with increasing number of elements are only obtained for the quadrangular elements. These results suggest that, in this model, the element's shape has a higher influence than the partition's morphology in the final result.

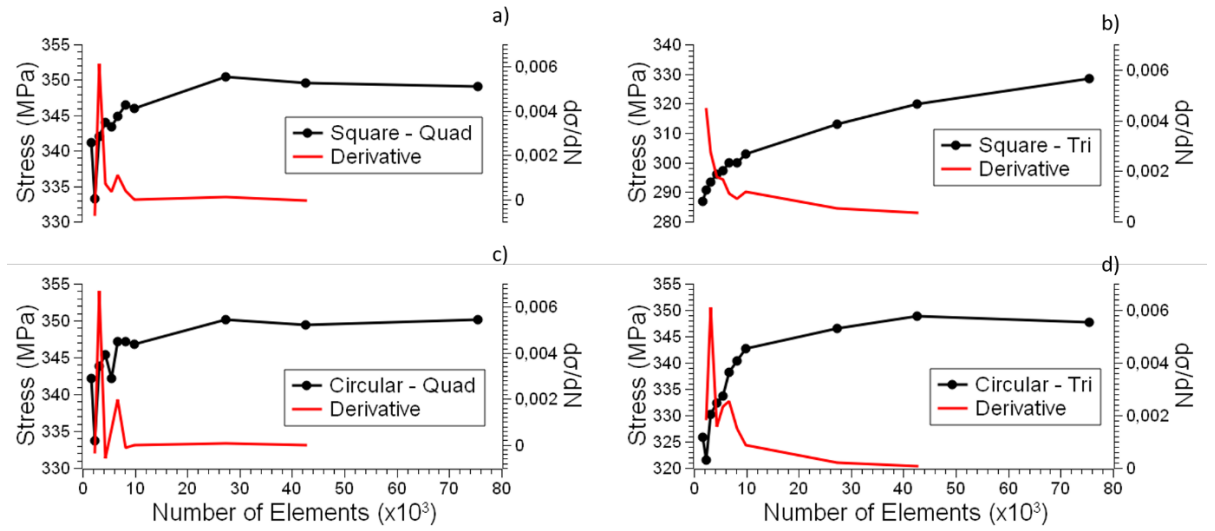

Figure 34 – Von Mises stress curves and their respective derivative plotted against the number of elements present in the Body's mesh: a) Square partition with quadrangular elements; b) Square partition with triangular elements; c) Circular partition with quadrangular elements; d) Circular partition with triangular elements.

The data on equivalent plastic strain (Figure 35) follows the same trend observed on stress plots analysed before. For the circular partition with triangular elements strain quickly increases with the number of elements. For the square partition and triangular elements, the stabilization of strain is only obtained after 40000 elements. For quadrangular elements, with both circular and square partition, strain values reach a plateau at 10000 elements. Results from equivalent plastic strain (EPS) suggest that quadrangular elements have higher stability and better agreeability than triangular elements.

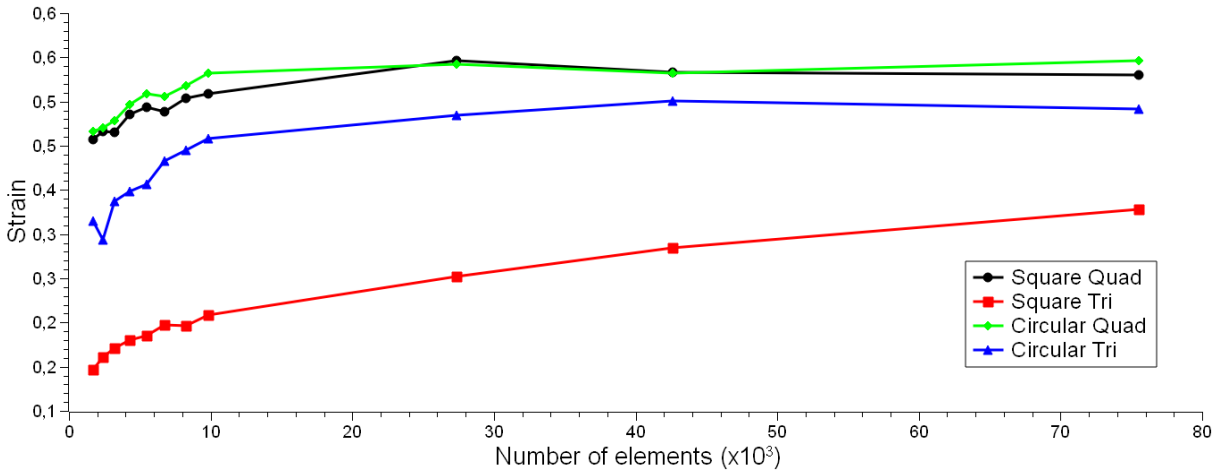

Figure 35 – Equivalent plastic strain (EPS) plotted against the number of elements present in the mesh.

In Figure 36, the contact pressure (CP) is plotted against the number of elements in the mesh. This parameter remains approximately constant, at 766 MPa, for quadrangular elements, with either partition. The same does not hold for the triangular elements mesh with the circular partition showing local maxima values of pressure with great differences in magnitude, for a low number of elements. The square partition with triangular elements has a lower variation of contact pressure, but still significant when compared to the quadrangular elements experiments.

The values of contact pressure in Figure 36 represent the maximum for this parameter at the end of the indentation step, since there is no contact afterwards.

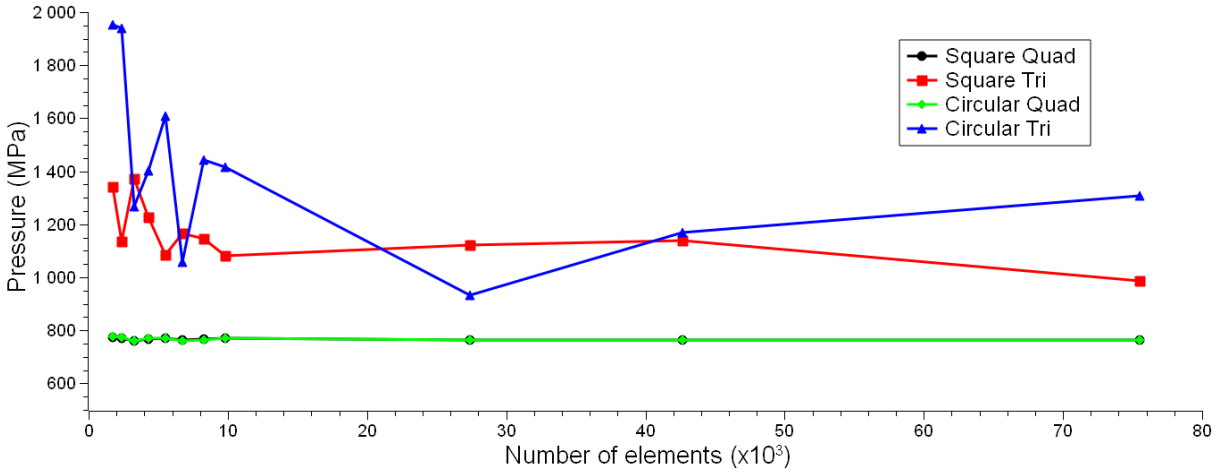

Figure 36 - Contact pressure (CP) plotted against the number of elements in the mesh.

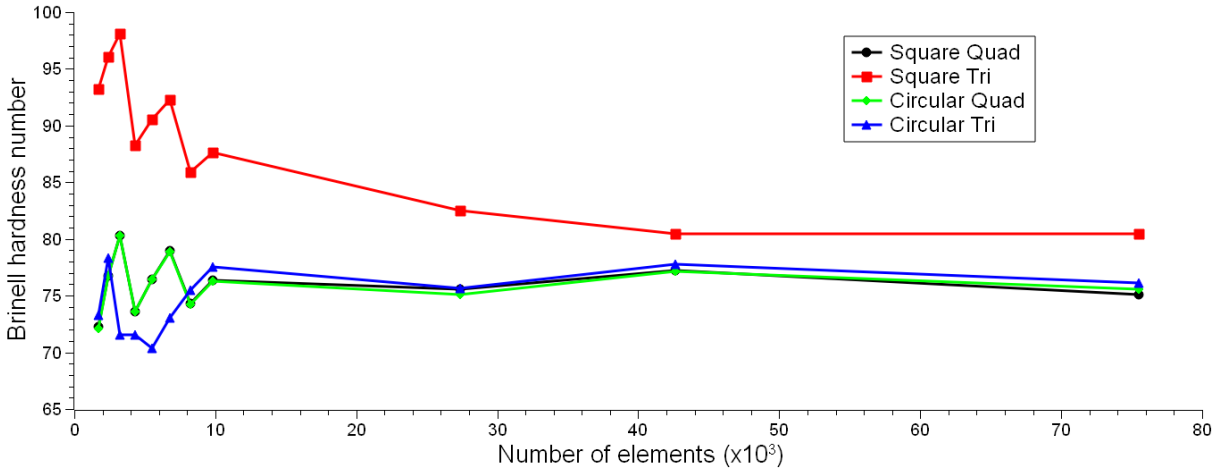

Figure 37 - Brinell hardness number plotted against the number of elements in the mesh.

The reported values of BHN for copper range from 70 to 100 [50]. The results obtained from the mesh study simulations (Figure 37) are within the expected values, confirming the validity of the simulation. For a square partition with a mesh of triangular elements the hardness number decays when the number of elements increases, converging to approximately 81. The remaining three curves plotted in Figure 37 exhibit the same behaviour with very similar hardness values.

Based on the results from the mesh study, it was decided that the model for the porous body would have a square partition with 42643 quadrangular elements (CAX4R). This configuration shows the highest stability in terms of stress and strain among those studied.

- Pile-up and sink-in effects

As previously described in section 2.4.2, Brinell hardness tests are carried out by indenting the sample with a tungsten carbide ball indenter. Depending on the properties of the tested materials, pile-up or sink-in effects might occur. This affects the measured indented area and consequently the hardness number. With pile-up effects the contact radius increases, thus decreasing the BHN. The opposite occurs for sink-in effects [59].

Brinell indenters, unlike like Vickers' or Knoop's, have no edges, and for this reason it is more difficult to measure the indentation size left on the sample, thus influencing the material's hardness. Because the body will deform according to its nodes, the mesh can also be a source of error regarding the BHN.

5.1.8. Material Model Comparison

In the previous simulations the Johnson-Cook model of plasticity (hereon referred to as classical plasticity model (CPM)) was used to study the mesh of the body.

The purpose of this work is to study the Brinell hardness test simulation on porous bodies. To do so, the GTN model will be used. The GTN model allows the variation of the relative density of the material from 1 (which represents a fully dense material) to 0.9 (that represents a material with 10% of porosity). Due to this, it is necessary to compare the GTN model at 0% porosity with the CPM model, to assess its validity.

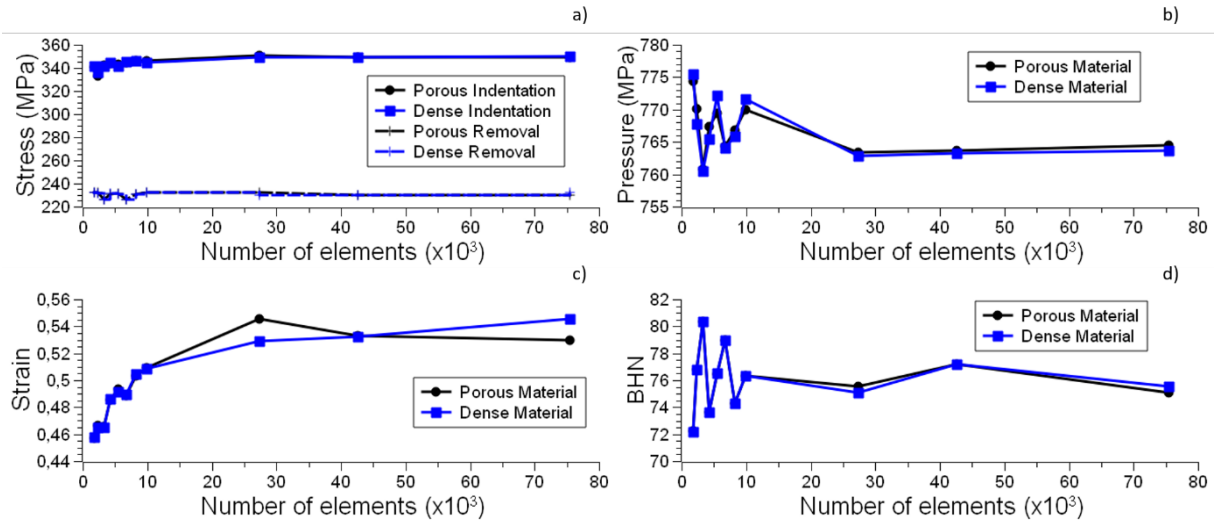

Figure 38 - Comparison between the two material models, GTN and CPM, regarding: a) the von Mises stress, b) contact pressure c) equivalent plastic strain, and d) Brinell harness number (BHN).

The results of the validation study are depicted on Figure 38 with respect to stress, strain, contact pressure and hardness. Regardless of the number of elements, the comparison was carried out for all the parameters.

The stress, from both steps (indentation and removal) was identical for the two models, regardless of the number of elements. For contact pressure, the two models start to converge for a higher number of elements, above 10 000. The equivalent plastic strain (EPS) values increase with the number of elements for both models with a local maximum for the GTN model, at approximately 27 000 elements, which is not present in the CPM model. Both models show approximately the same EPS and BHN for 42643 elements. Table 12 displays the difference between the two models at the end of the removal step.

Table 12 – Difference between the CPM and the GTN model for the tested parameters (with 42643 CAX4R elements). The results are displayed in percentage.

	Step 1 - Indentation		Step 2 - Removal		Hardness
Number of Elements	Max EPS	Max S	Max CP	Max S	BHN
42643	-0.13153	0.02860	-0.06551	0.13038	-0.01067

For the selected testing configuration, the results reveal that the two models are similar, since the maximum difference found is below 0.14%.

These results validate the applicability of the GTN model, making it possible to test and assess values of stress, strain, contact pressure and hardness for porosities up to 10%.

5.1.9. Simulation time

For the simulation time, three stages were defined: indentation, holding and removal. A 1 second indentation stage was defined, during which the indenter penetrates the sample. This is followed by the holding stage, when the indenter is kept stationary at full indentation depth for a minimum of 10 seconds. The final stage, removal, which lasts for 1 second, comprises the indenter is removal from the body, thus ending the hardness test.

The simulation time was set as described by the Brinell Hardness Test Standards [31].

5.2. Results

The final simulation aims to study the influence that the applied load has on the material's hardness, for different fixed values of porosity, establishing a correlation between the applied load and measured hardness. Three loads were applied: 1500, 1000 and 500 kgf; one diameter was used (10mm) and relative density (porosity) varied from 1 to 0.9 with 0.01 increments.

The other goal of the simulation is to evaluate how the material behaves for a given F/D^2 ratio and relative density. Two F/D^2 ratios were selected: 10 and 5 kgf/mm^2; three indenter diameters were used: 2.5, 5 and 10 mm; with three relative densities: 1, 0.95 and 0.9, and the load resulted from the F/D^2 ratio.

All the selected conditions resulted in a total of 57 different simulations.

Five valuable output variables were identified: Von Mises stress (S), which assesses the stress applied on the body; equivalent plastic strain (EPS), that provides information on the body's deformation; contact

pressure (CP), as endured by the body; void volume fraction (VVF) and void volume fraction growth (VVFG), which relate to the void amount and closure.

The Brinell hardness number is calculated with equation (4). For the indenter's diameter, the distance from the symmetry axis to the node that maintains its original relative position is measured, as described in section 5.1.7.

5.2.1. Porosity influence in the Hardness test

To assess the influence of porosity and load on Brinell hardness value, loads of 1500, 1000 and 500 kgf were selected. Figure 39 plots Brinell hardness number (BHN) versus relative density (RD).

For a RD of 1 (which corresponds to 0% of porosity), the material has a hardness of 77.18 BHN, 74.62 BHN and 71.99 BHN for the respective loads 1500, 1000 and 500 kgf. For a RD of 0.9 (10% porosity), the Brinell hardness of the material is now 59.09 BHN, 55.50 BHN and 52.04 BHN for the same loads (in the same order).

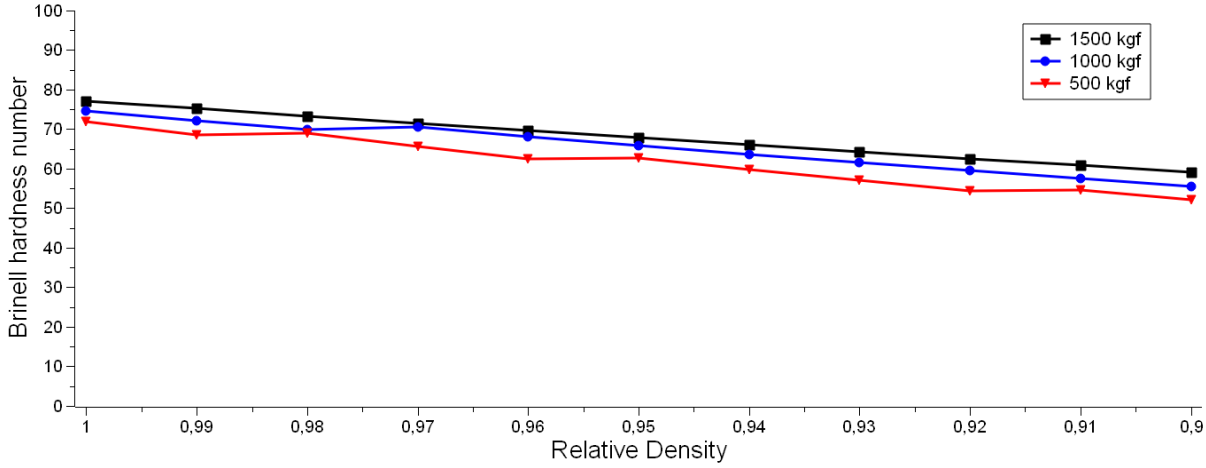

Figure 39 - Brinell hardness number plotted against the relative density for the three different load configurations tested (1500, 1000 and 500 kgf).

A linear decrease in BHN with a decrease in RD is suggested by the fitting equations (13) to (15).

$$BHN_{500} = 199.16x - 127.56 \quad R^2 = 0.9798 \tag{13}$$

$$BHN_{1000} = 189.05x - 114.26 \quad R^2 = 0.9871 \tag{14}$$

$$BHN_{1500} = 180.16x - 103.22 \quad R^2 = 0.9995 \tag{15}$$

The difference in hardness, due to the increase of relative density, for 1500, 1000 and 500 kgf applied loads, corresponds to 18.09 BHN, 19.12 BHN and 19.95 BHN respectively. Also, lower applied loads produce lower BHN. This could be due to the lack of material (increasing porosity percentage) beneath the indenter. Therefore, for the same volume there is less copper mass on which stress can be dissipated, promoting higher deformation, hence lower hardness.

A relationship between BHN and VVF, for any applied load, is proposed in equation (16).

$$BHN = 74.9 \cdot \left(\frac{F}{D^2}\right)_h^{-0,065} - 187.7 \cdot VVF \cdot \left(\frac{F}{D^2}\right)_h^{-0,215} \qquad (16)$$
$$R^2 = 0.9998$$

BHNs are corrected taking in account the F/D² ratio used. Considering that 10 represents a recommended F/D² ratio for copper and copper alloys a dimensionless homologous ratio, $(F/D^2)_h$, is defined as $(F/D^2)_h = F/(10 \cdot D^2)$. Figure 40, represents $BHN \cdot (F/D^2)_h{}^{0.065}$ as a function of a of the homologous volume void fraction $VVF_h = VVF \cdot (F/D^2)_h{}^{-0.15}$.

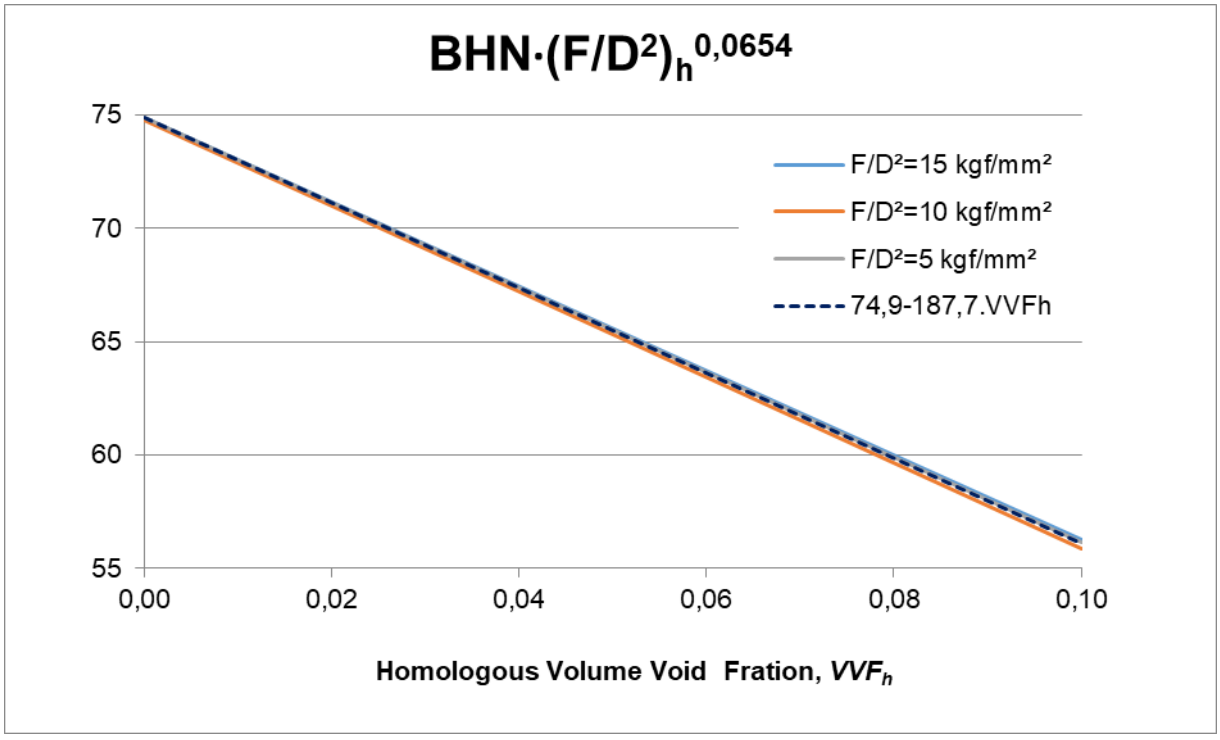

Figure 40 – Brinell Hardness simulation results for all load conditions. D=10mm.

Figure 41 plots Von Mises stress for the indentation and removal steps, CP and EPS against the relative density of the material.

For all applied loads, stress decreases when the relative density decreases (increase in porosity). The difference of stress (recorded at the end of the indentation step) between 0 and 10% porosity is 35.8,

56.9 and 68.5 MPa for the 1500, 1000 and 500 kgf applied loads, respectively. This difference increases when the load decreases from 1500 to 500 kgf.

For the removal step, these differences are 3.2, 23.9 and 58.5 MPa, respectively.

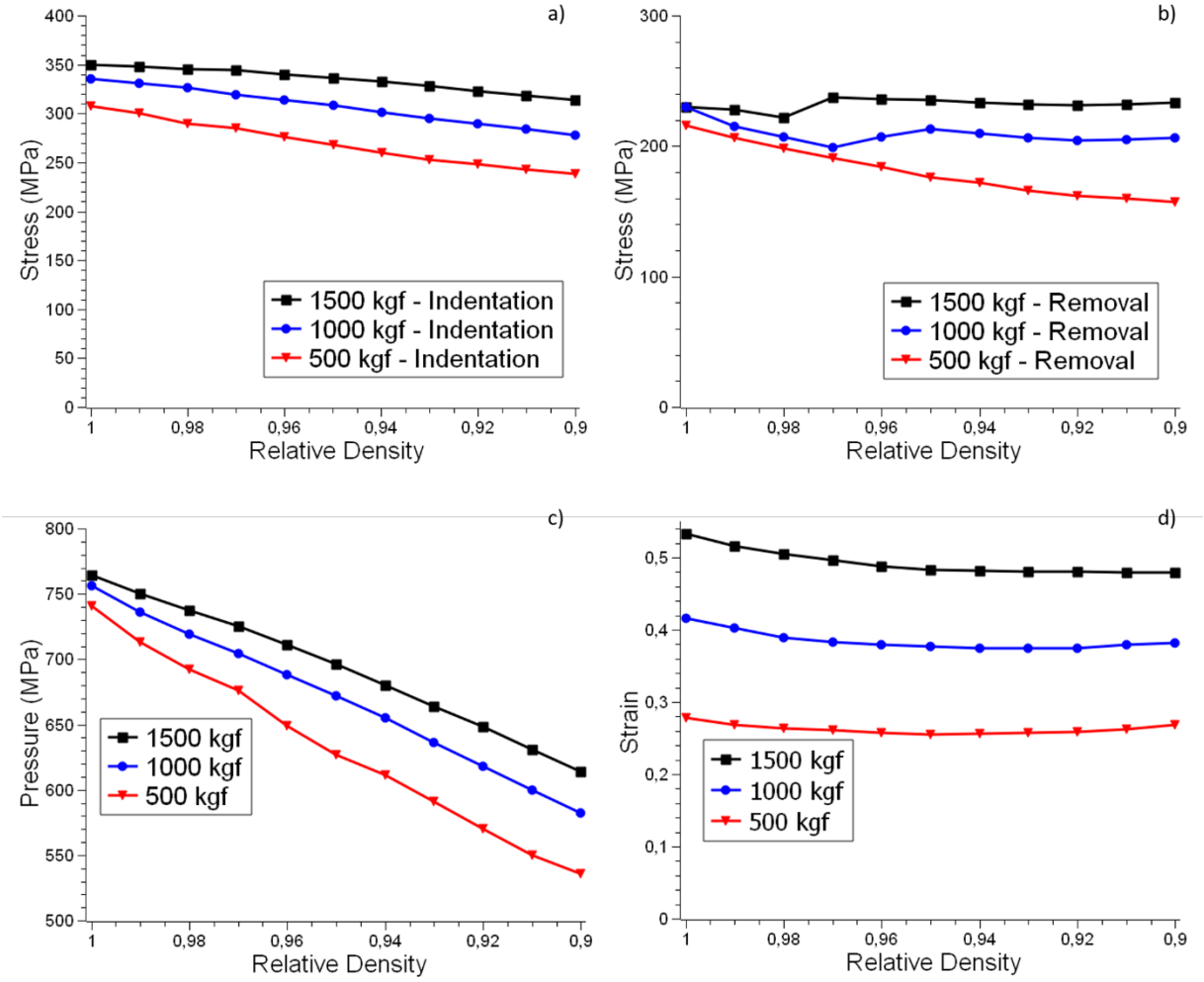

Figure 41 - Maximum values of Von Mises stress at a) indentation and b) removal, c) contact pressure and d) equivalent plastic strain.

With increasing porosity, there is less material to support the applied load, and so, the stress required to induce plastic deformation is lower. It is predictable that for a same porosity percentage, lower loads induced lower stress values on the material.

For the Von Mises stress at removal it is observed that some instabilities occur at values of RD between 0.98 and 0.96.

Equations (17) to (19), obtained by fitting trendlines to the data, are proposed for the variation of the Von Mises stress (in MPa) at full indentation depth with relative density (RD). The coefficient of determination (R^2), used as an acceptance criterion, shows that the equations are a good fit for the data.

$$Sind_{500} = 1961.5 \cdot (RD)^2 - 3025 \cdot RD + 1371.2 \qquad R^2 = 0.9979 \qquad (17)$$

$$Sind_{1000} = -322.84 \cdot (RD)^2 + 1196.9 \cdot RD - 538.08 \qquad R^2 = 0.9989 \qquad (18)$$

$$Sind_{1500} = -2032.6 \cdot (RD)^2 + 4229.6 \cdot RD - 1847.1 \qquad R^2 = 0.9990 \qquad (19)$$

CP decreases with the increase in porosity, but with a higher difference between the minimum and maximum values of porosity than the one recorded for stress, which correspond to 149, 174 and 205 MPa, for 1500, 1000 and 500 kgf loads respectively. The values of equivalent plastic strain (EPS) also decrease from 1 to 0.9 relative density with the magnitudes: 0.0544, 0.0342 and 0.0098 for the 1500, 1000 and 500 kgf loads, respectively. Regarding their initial values (for a relative density of 1) the EPS shows lower but little deviation.

Both contact pressure and VVFG present negative slopes in their respective figures. This indicates that the applied load is not only responsible for plastically deforming the material but also for compacting voids beneath the indenter. Since the applied load is closing the voids while deforming the material at the same time, it would be expected that both strain and stress would maintain a decreasing but steady value with increasing porosity as observed in Figure 41.

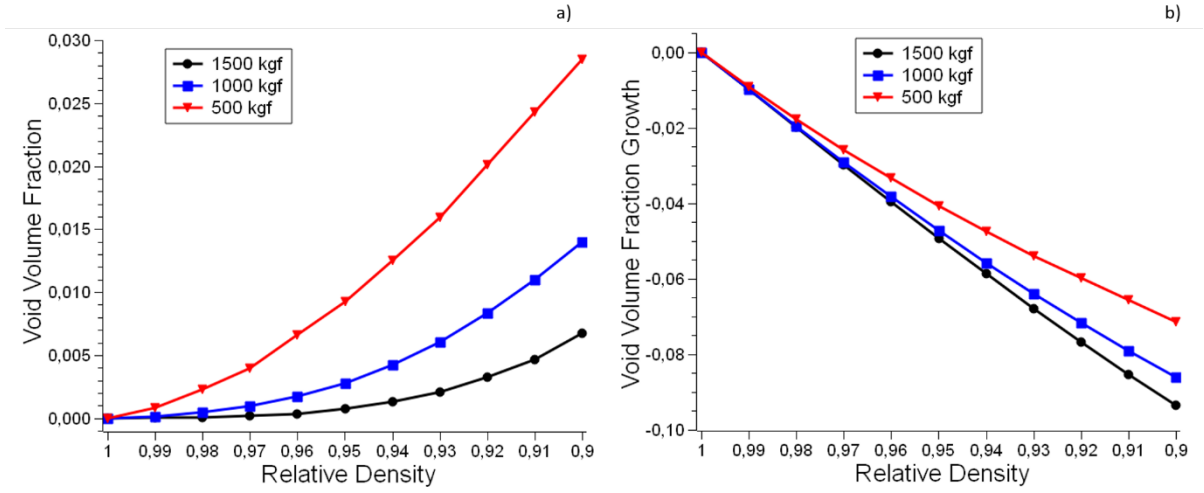

Figure 42 – VVF and VVFG variables, a) and b) respectively, plotted against the relative density of the copper body for three applied loads: 1500, 1000 and 500 kgf.

Figure 42 shows the variation of VVF and VVFG parameter with the relative density of a copper body for the applied loads.

The increase of VVF with decreasing relative density (Figure 42-a) is mathematically expressed by the parabolic fitting equations (20) to (22).

$$VVF_{500} = 2.0038 \cdot (RD)^2 - 4.0978 \cdot RD + 2.0937 \qquad R^2 = 0.9995 \qquad (20)$$

$$VVF_{1000} = 1.6921 \cdot (RD)^2 - 3.351 \cdot RD + 1.6592 \qquad R^2 = 0.9990 \qquad (21)$$

$$VVF_{1500} = 1.0596 \cdot (RD)^2 - 2.0738 \cdot RD + 1.0146 \qquad R^2 = 0.9892 \qquad (22)$$

Void growth versus relative density graph (Figure 42-b) has a negative slope due to the compaction of the pre-existing voids in the region beneath the indenter where the indented region underwent plastic deformation.

This compaction behaviour follows a polynomial trend. Equations (23) to (25) are proposed for the relationship between void growth and relative density, ensuring a perfect fit to the plots, since the coefficient of determination equals 1.

$$VVFG_{500} = 2.0035 \cdot (RD)^2 - 3.0972 \cdot RD + 1.0935 \qquad R^2 = 0.9999 \qquad (23)$$

$$VVFG_{1000} = 1.6904 \cdot (RD)^2 - 2.3479 \cdot RD + 0.6577 \qquad R^2 = 1 \qquad (24)$$

$$VVFG_{1500} = 1.0275 \cdot (RD)^2 - 1.0122 \cdot RD - 0.0151 \qquad R^2 = 1 \qquad (25)$$

- Summary

Through this study it was verified that the BHN decreases linearly with relative density for all tested loads. Equations (13) to (15) are proposed to describe the BHN variation with relative density. All Brinell hardness simulation results can be expressed by equation (16), if F/D^2 ratio is considered, for copper, when VVF ranges from 0 to 0.1.

The Von Mises stress decreases with decreasing relative density, since for the same volume there is less material to support the applied load. Equations (17) to (19) are proposed for the relationship between Von Mises stress and relative density.

The EPS maintains the same trend with relative density for all the applied loads. Higher loads induce higher values of EPS. Lower applied loads exhibit higher differences between 0 and 10% porosity.

For increasing porosity, with a higher applied load VVF and VVFG parameters present the lowest value, since there is more compaction due to higher plastic deformation. Equations (20) to (22) are proposed to describe the variation of VVF with relative density. The relationship between VVFG and the relative density is provided by the proposed equations (23) to (25).

5.2.2. Indenter size and load influence on the hardness test

To evaluate load/indenter size ratio influence on BHN, the F/D^2 that roughly represents the applied stress, must be kept the same when varying the indenter's size. Two F/D^2 ratios were selected, 5 and 10 kgf/mm², for three different indenter size diameters: 2.5, 5 and 10 mm. For each diameter three different porosity percentages (P) were used: 0%, 5% and 10%. For this study, the Von Mises maximum stress and the BHN were analysed.

- Von Mises Stress

The Von Mises stress variation with the diameter of the indenter is represented in Figure 43.

For a F/D^2 ratio of 10 kgf/mm² (Figure 43 a) and c)) the stress at full indentation and removal decreases with increasing porosity, just as discussed in the previous section. This behaviour is attributed to the fact that there is less material to support the applied load, therefore, the stress required to deform the material decreases when porosity increases.

When the indenter's diameter varies from 2.5 to 10mm, the stress at full indentation increases, reaching eventually a threshold that depends on the porosity: 335, 308 and 279 MPa for 0, 5 and 10% porosity, respectively. This increase is maximum for a fully dense material (0% porosity).

Under a lower F/D^2 ratio (Figure 43 b) and d)) for 0 and 5% porosity the material's behaviour follows the 10 kgf/mm² F/D^2 ratio trend. For 10% porosity, there is an irregular variation with respect to the indenter diameter, for a 5-mm diameter. This could suggest that the model is not reliable for higher porosities at lower applied loads.

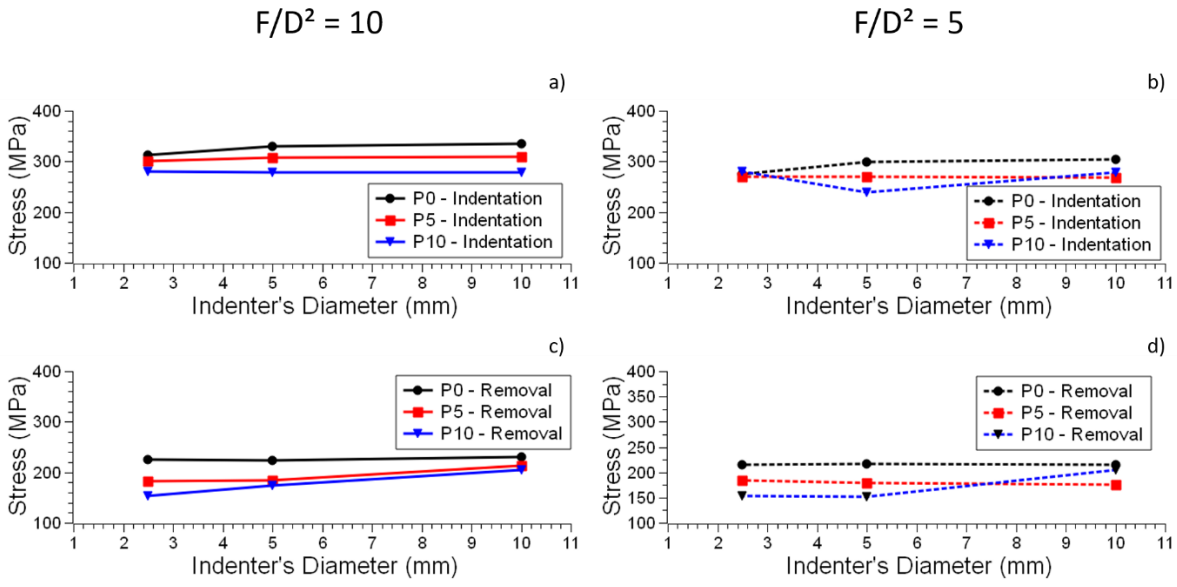

Figure 43 - Maximum values of Von Mises stress variation with the indenter's diameter, at the end of the indentation and removal steps, for F/D^2 ratios of 10 and 5 kgf/mm², with three porosity levels (0, 5 and 10%).

As discussed in section 5.2.1, the stress at removal is lower for higher porosity percentages. It increases with increasing indenter's diameter.

Figure 44 compares the stress and relative density for different diameters, at the indentation and removal steps. For a 10 kgf/mm² F/D² ratio, the stress tends to decrease linearly with relative density. This is observed for all the indenter diameters for both the indentation and removal steps.

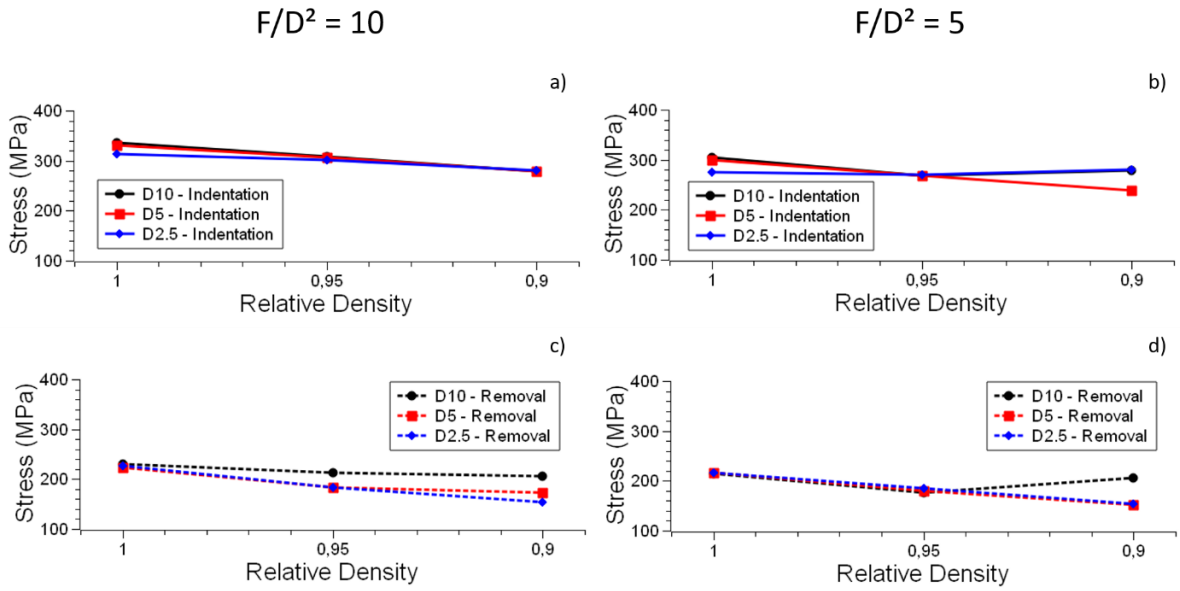

Figure 44 – Correlation between maximum Von Mises stress and relative density, at the end of the indentation (a) and b)) and removal (c) and d)) steps.

For the 5 kgf/mm² F/D² ratio no general trend could be observed. The biggest deviations are observed for a relative density value of 0.9. At such relative density, one is carrying test at the edge of the model's applicability. This could be the cause of such deviations.

The lack of consistency verified for a small F/D² ratio suggests that the model cannot be used under low values of applied load, as already suggested.

- Brinell hardness

The influence of the indenters' size on BHN is represented in Figure 45 for the tested F/D² ratios (5 and 10 kgf/mm²).

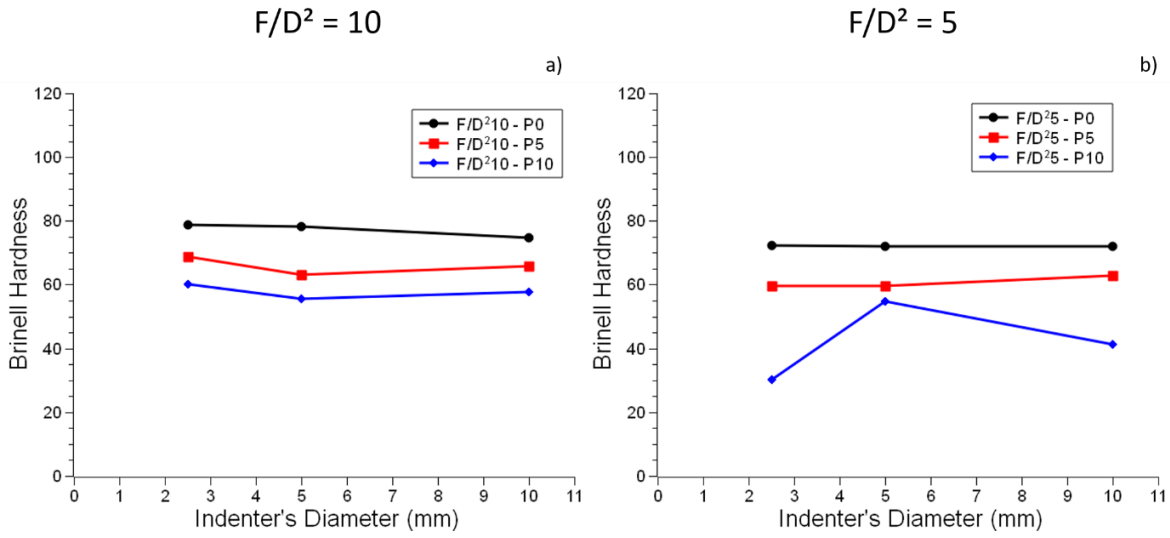

Figure 45 - Brinell hardness variation with indenter's diameter for three porosity levels (0, 5 and 10%) and two F/D² ratios: a) 10 kgf/mm² ratio; b) 5 kgf/mm² ratio.

The results show that for the highest porosity the results are not stable, particularly for a F/D² ratio of 5 kgf/mm². This suggests some application limits for the used simulation and GTN model, as previously verified for the Von Mises stress.

Table 13 summarizes the data for the F/D² ratios of 10 and 5 kgf/mm².

Table 13 - Mean Brinell hardness number for both F/D² ratios, for all the tested porosity percentages.

	Porosity		
F/D² ratio	0%	5%	10%
10	76.03 ± 2.86	68.23 ± 5.10	56.38 ± 3.48
5	68.37 ± 6.89	60.36 ± 1.62	43.53 ± 16.40

Higher values of BHN are observed for a F/D² ratio of 10 kgf/mm², for all the tested porosity percentages.

For high applied loads (F/D² ratio of 10 kgf/mm²), the indenter diameter has little influence on the BHN of a porous copper body.

- Pile-up and sink-in effects

Figure 46 shows the final indentation imprints that remained in the material after the hardness test. The horizontal normalized distance from the symmetry axis to the end of the partition's edge is represented by the ratio r/R, while the ratio y/R represents the normalized distance from the initial indenter's top to the edge of the square partition.

The simulations results show that only pile-up occurs. The amout of pile-up decreased with porosity. When a sample is indented, material flows according to the path of least resistance. The region

immedeatly around the indenter will flow more easily outwards. When the indented material is porous, the voids are closed through plastic deformation. This way the pile-up effect is compensated by the sample densification.

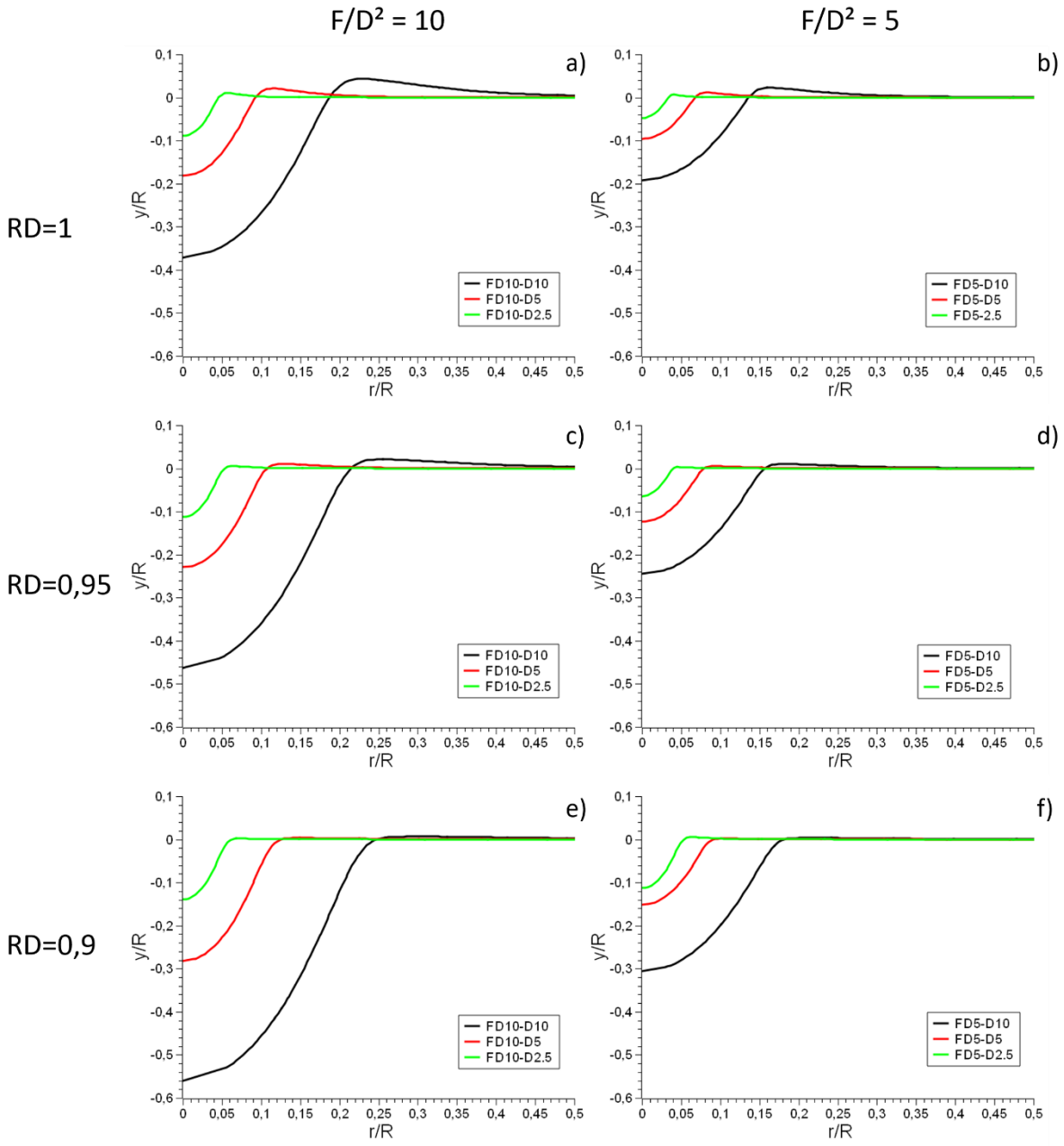

Figure 46 - Indentation imprints on the sample after the hardness test. F/D² ratios of 10 and 5 kgf/mm² were tested, as well as three porosity percentages (0, 5 and 10%).

From Figure 46 it is observed that for a F/D² ratio of 10 kgf/mm² a higher indentation depth is achieved. The indentation depth increases when porosity increases.

- Summary

This study was carried out to evaluate the influence that the load/indenter's size ratio has on BHN. For a 10 kgf/mm² F/D^2 ratio, the Von Mises stress at the end of the indentation step decreases when the relative density decreases, since there is less material to support the applied load. When the indenter size increases so does the Von Mises stress at the end of the indentation step. This is more preponderant for low porosity bodies. At the end of the removal step, the Von Mises stress decreases when relative density decreases. For a 5 kgf/mm² F/D^2 ratio, irregular variations are observed for a relative density of 0.9. No trend was observed for this value of F/D^2 when relative density decreased. This suggests that the model has application limits for lower applied loads at high porosity contents (10%).

At a F/D^2 ratio of 10 kgf/mm², the indenter's size has little influence on the BHN. It is observed that for 0% and 5% porosity there is a difference of 10 BHN between the two tested F/D^2 ratios. Under 5kgf/mm² and for 10% porosity the model shows low data consistency, thus suggesting that the GTN model has limitation for these conditions, as already mentioned.

Only pile-up effects were observed, for all the simulations. It has more influence in the BHN measurement for less porous materials, since for high porosity bodies (10% porosity) the pile-up effect is compensated by the void compaction during indentation.

6. Conclusions and further work

In this section work's conclusions are presented along with suggestions for further work.

6.1. Powder Spheroidization

This work studies the influence of temperature, copper-graphite ratio (CGR), graphite powder size, applied stress and time on powder spheroidization.

Graphite powder size influence on spheroidization could not be assessed because not enough significant samples could be retrieved from the separation process.

The particle's shape of all the observed samples changed after the spheroidization process. Due to a high standard deviation, it is not possible to conclude the influence of each parameter on the spheroidization process.

Separation of copper and graphite powders was not feasible using only water as suspension medium and sonication. A hydrochloric aqueous solution was instead tested as a separation medium. This method effectively separates the two powders, but also modifies the particles morphology, because copper is corroded in the presence of chlorine ions.

Some samples exhibited particles with cubes on their surfaces after the separation procedure. No similar results were found in literature, thus further word on this topic is suggested to understand this occurrence.

The estimated shape factor for the initial dendritic powder was 2.67±0.54. A best shape factor of 1.55±0.46 is suggested for test carried out at 1100ºC for 30 minutes, under low applied stress with graphite KS4.

6.2. Simulations

Hardness test of porous copper bodies was simulated using a FEM approach. The Gurson-Tvergaard-Needleman (GTN) material model was used to simulate the porous body. The GTN and the Johnson-Cook models were matched against each other, and a good correlation was found for a fully dense material. Quadrangular elements were chosen for the body mesh since those were found to adapt more easily to the body deformation than triangular elements.

The influence of porosity and the load/indenter's size ratio, F/D^2, on Brinell hardness number, BHN, was studied. BHN decreases linearly with relative density for all tested loads. Equations (13) to (15) are proposed to describe the BHN variation with relative density. Equation (16), $, BHN = 74.9 \cdot$

$(F/D^2)_h{}^{-0.065} - 187.7 \cdot VVF \cdot (F/D^2)_h{}^{-0.215}$, is proposed to describe the variation of BHN with VVF, for any given F/D² ratio.

The Von Mises Stress, the equivalent plastic strain, the volume void fraction and the volume void fraction growth all present a parabolic dependence with relative density.

Von Mises stress decreases with decreasing relative density, since for the same volume there is less material to support the applied load. The equivalent plastic strain, EPS, maintains the same trend with relative density for all the applied loads. Higher loads induce higher values of EPS.

For increasing porosity, the volume void fraction, VVF, and the volume void fraction growth, VVFG, present the lowest value for a higher applied load, since there is more compaction due to higher plastic deformation.

Two F/D² ratios, 10 kgf/mm² and 5kgf/mm², were used to study the influence of this parameter and of the indenter size on BHN. For a F/D² ratio of 10 kgf/mm², the indenter's size has little influence on BHN. For 0% and 5% porosity, the difference between the two tested F/D² ratios is approximately 7.8 BHN (11.4%). For 5kgf/mm² and 10% porosity the model shows low data consistency, suggesting that the developed model has limitation for these conditions.

The pile-up, up flow of material around the indentation periphery, is present as a result of the FEM experiments. Results show that pile-up effect is more significant for low porosity samples. For higher porosities, the void compaction compensates this effect. Higher F/D² ratios increase the pile-up height.

The created model provided more consistent results for simulations with both high diameters and F/D² ratios for all the tested variables.

6.3. Further work

Copper powder spheroidization was not completely successful. To better investigate this process's capabilities the following suggestions are proposed:

- Sieve the samples to spheroidize particles within a narrow powder distribution size;
- Test spheroidization with graphite flakes of smaller dimensions;
- Develop a method to separate copper from graphite without altering the particle's morphology;
- Carry out particle size analysis after separation with Coulter equipment;
- Study the formation of cubes on the surface of oxidized copper particles.

The finite element computational model can be further developed and tested with the following suggestions:

- Carry out experimental porosity tests on sintered copper bodies with spherical particles;
- Determine hardness values for sintered copper bodies with controlled porosity to correlate experimental data with the FEM simulation;

7. References

[1] V. V Konchits, M. Braunovic, and N. K. Myshkin, “Fundamentals of Electrical Contacts,” 2006.

[2] ASM International Handbook, “Properties and selection: Nonferrous alloys and special-purpose materials,” *ASM Met. Handb.*, vol. 2, p. 1300, 1990.

[3] H. Dai, S. Wang, G. Zhu, and P. Zeng, “A new route for manufacturing monodispersed spherical copper particles for electronic applications,” *Mater. Lett.*, vol. 118, pp. 173–175, 2014.

[4] C. M. Lewandowski, N. Co-investigator, and C. M. Lewandowski, “Powder Metal Technologies and Applications,” *ASM Int. Mater. Park. OH*, vol. 7, p. 2762, 2015.

[5] J. M. Capus, *Metal Powders*. Elsevier Advanced Technology, 2005.

[6] G. S. Upadhyaya, *Powder Metallurgy Technology*. Cambridge International Science Publishing, 1997.

[7] V. Folea and E. Cahill, “Metallurgy made in and for Europe - The perspective of producers and end-users roadmap,” 2014.

[8] R. DeFrain and C. Mumau, “Considerations for Metal Powders used in Additive Manufacturing,” in *OMTEC 2017*, 2017.

[9] M. Boz and M. Hasheminiasari, “The effect of process parameters on copper powder particle size and shape produced by electrolysis method,” *Steel Compos. Struct.*, vol. 15, no. 2, pp. 151–162, 2013.

[10] P. Atkins and J. Paula, *Physical chemistry*. Oxford University Press, 2006.

[11] I. Egry, E. Ricci, R. Novakovic, and S. Ozawa, “Surface tension of liquid metals and alloys-Recent developments,” *Adv. Colloid Interface Sci.*, vol. 159, no. 2, pp. 198–212, 2010.

[12] A. Adamson and A. Gast, *Physical Chemistry Of Surfaces*. Wiley, 1997.

[13] T. Young, “An Essay on the Cohesion of Fluids,” *Philos. Trans. R. Soc. London*, vol. 95, pp. 65–87, 1805.

[14] G. Bracco and B. Holst, *Surface science techniques*, vol. 51, no. 1. 2013.

[15] C. Lei, H. Huang, Y. Huang, Z. Cheng, S. Tang, and Y. Du, “In-situ de-wetting assisted fabrication of spherical Cu-Sn alloy powder via the reduction of mixture metallic oxides,” *Powder Technol.*, vol. 301, pp. 356–359, 2016.

[16] K. Takagi, S. Masuda, H. Suzuki, and A. Kawasaki, “Preparation of Monosized Copper Micro Particles by Pulsated Orifice Ejection Method,” *Mater. Trans.*, vol. 47, no. 5, pp. 1380–1385, 2006.

[17] Z. Spârchez, “Fabrication of metal powders having spherical shape particles (an overview),” *Adv. Mater. Res.*, vol. 23, pp. 95–98, 2007.

[18] F. Nilsén, I. Aaltio, Y. Ge, T. Lindroos, and S. P. Hannula, “Characterization of Gas Atomized Ni-Mn-Ga Powders,” *Mater. Today Proc.*, vol. 2, pp. S879–S882, 2015.

[19] R. I. L. Howells, G. R. Dunstan, and C. Moore, “Production of gas atomised metal powders and their major industrial uses,” *Powder Metall.*, vol. 31, no. 4, 1988.

[20] Z. Cheng, C. Lei, H. Huang, S. Tang, and Y. Du, “The formation of ultrafine spherical metal powders using a low wettability strategy of solid-liquid interface,” *Mater. Des.*, vol. 97, pp. 324–330, 2016.

[21] C. Lei, H. Huang, Z. Cheng, S. Tang, and Y. Du, “Mono-disperse spherical Cu-Zn powder fabricated via the low wettability of liquid/solid interface,” *Appl. Surf. Sci.*, vol. 357, pp. 167–171, 2015.

[22] C. Lei, H. Huang, Z. Cheng, S. Tang, and Y. Du, “Fabrication of spherical Fe-based magnetic powders via the in situ de-wetting of the liquid-solid interface,” *RSC Adv.*, vol. 6, no. 5, pp. 3428–3432, 2016.

[23] C. Lei, H. Huang, Z. Cheng, S. Tang, and Y. Du, “Mono-disperse spherical Cu-Zn powder fabricated via the low wettability of liquid/solid interface,” *Appl. Surf. Sci.*, vol. 357, pp. 167–171, 2015.

[24] J. Abrahamson, “The surface energies of graphite,” *Carbon N. Y.*, vol. 11, no. 4, pp. 337–362, 1973.

[25] B. J. Keene, “Review of data for the surface tension of pure metals,” *Int. Mater. Rev.*, vol. 38, no. 4, pp. 157–192, 1993.

[26] P. D. Ownby and J. Liu, “Surface energy of liquid copper and single-crystal sapphire and the wetting behavior of copper on sapphire,” *J. Adhes. Sci. Technol.*, vol. 2, no. 1, pp. 255–269, 1988.

[27] D. A. Mortimer and M. Nicholas, “The wetting of carbon by copper and copper alloys,” *J. Mater. Sci.*, vol. 5, no. 2, pp. 149–155, 1970.

[28] G. A. López and E. J. Mittemeijer, “The solubility of C in solid Cu,” *Scr. Mater.*, vol. 51, no. 1, pp. 1–5, 2004.

[29] J. N. Reddy, “An Introduction to the Finite Element Method.” p. 684, 1993.

[30] M. Deville, R. Michel, and B. Michel, *Numerical Modeling in Materials Science and Engineering*. 2003.

[31] ASTM International, “Standard Test Method for Brinell Hardness of Metallic Materials 1,” *ASTM*, vol. E10-15, pp. 1–32, 2014.

[32] ASM Handbook Committee, “Mechanical Testing and Evaluation,” in *ASM Handbook*, vol. 8, 2000, p. 2235.

[33] T. H. Courtney, *Mechanical behavior of materials*. 2000.

[34] A. Demir and F. O. Sonmez, “Prediction of Brinell Hardness Distribution in Cold Formed Parts,” *J. Eng. Mater. Technol.*, vol. 126, no. 4, p. 398, 2004.

[35] P. Grau and G. Berg, “Meyer´s hardness law and its relation to other measures of ball hardness tests,” *Cryst. Res. Technol.*, vol. 32, no. 1, pp. 149–154, 1997.

[36] Y. Tirupataiah and G. Sundararajan, “On the constraint factor associated with the indentation of work-hardening materials with a spherical ball,” *Metall. Trans. A*, vol. 22, no. 10, pp. 2375–2384, 1991.

[37] A. K. Bhattacharya and W. D. Nix, “Finite element simulation of indentation experiments,” *Int. J. Solids Struct.*, vol. 24, no. 9, pp. 881–891, 1988.

[38] Z. Chen, X. Wang, A. Atkinson, and N. Brandon, “Spherical indentation of porous ceramics: Elasticity and hardness,” *J. Eur. Ceram. Soc.*, vol. 36, no. 6, pp. 1435–1445, 2016.

[39] A. L. Gurson, “Continuum Theory of Ductile Rupture by Void Nucleation and Growth: Part I—Yield Criteria and Flow Rules for Porous Ductile Media,” *J. Eng. Mater. Technol.*, vol. 99, no. 1, pp. 2–15, 1977.

[40] Z. Chen, X. Wang, N. Brandon, and A. Atkinson, “Analysis of spherical indentation of porous ceramic films,” *J. Eur. Ceram. Soc.*, vol. 37, no. 3, pp. 1031–1038, 2016.

[41] M. Sabzevari, R. J. Teymoori, and S. A. Sajjadi, “FE modeling of the compressive behavior of porous copper-matrix nanocomposites,” *Mater. Des.*, vol. 86, pp. 178–183, 2015.

[42] V. Tvergaard, “Influence of voids on shear band instabilities under plane strain conditions,” *Int. J. Fract.*, vol. 17, no. 4, pp. 389–407, 1981.

[43] Beckman Coulter Inc., “Coulter LS series, Product Manual,” *Tecdoc Pn 4237214Ea*, no. 1. 2011.

[44] M. Hasegawa, “Ellingham Diagram,” in *Treatise on Process Metallurgy*, vol. 1, Elsevier Ltd., 2013, pp. 507–516.

[45] F. N. Ponnamperuma, M. T. Cayton, and R. S. Lantin, “Dilute hydrochloric acid as ab extractant for available zinc, copper ans boron in rice soils,” *Plant Soil*, vol. 61, no. 1981, pp. 297–310, 1981.

[46] B. Beverskog and I. Puigdomenech, “Pourbaix diagrams for the system copper-chlorine at 5–100 °C,” no. April, 1998.

[47] E. M. Sherif, “Corrosion Behavior of Copper in 0 . 50 M Hydrochloric Acid Pickling Solutions

and its Inhibition by 3-Amino-1 , 2 , 4-triazole," *Corrosion*, vol. 7, pp. 1884–1897, 2012.

[48] G. R. Johnson and W. H. Cook, "Fracture characteristics of three metals subjected to various strains, strain rates, temperatures and pressures," *Eng. Fract. Mech.*, vol. 21, no. 1, pp. 31–48, 1985.

[49] T. Seixas, "Development and modeling of mechanical alloying for production of copper matrix composite powders reinforced with alumina and graphite," Instituto Superior Técnico, 2016.

[50] Granta Design, "CES EduPack 2015." 2015.

[51] G. R. Johnson and W. H. Cook, "A constitutive model and data for metals subjected to large strains, high strain rates and high temperatures," *7th International Symposium on Ballistics*. pp. 541–547, 1983.

[52] D. Systèmes, "Abaqus Analysis User's Guide," in *Abaqus v6.14 Documentation*, 2014.

[53] D. Systèmes, "Abaqus/CAE User's Guide," in *Abaqus v6.14 Documentation*, 2014.

[54] P.-L. Larsson, S. Biwai_, and B. Storakers, "Analysis of Cold and Hot Isostatic Compaction of Spherical Particles," *Acta nzatw*, vol. 44, no. 9, pp. 3655–3666, 1996.

[55] S. Hao and W. Brocks, "The Gurson-Tvergaard-Needleman-model for rate and temperature-dependent materials with isotropic and kinematic hardening," *Comput. Mech.*, vol. 20, no. 1–2, pp. 34–40, 2014.

[56] M. Morehead, Y. Huang, and K. Ted Hartwig, "Machinability of ultrafine-grained copper using tungsten carbide and polycrystalline diamond tools," *Int. J. Mach. Tools Manuf.*, vol. 47, no. 2, pp. 286–293, 2007.

[57] ASTM Int., "Standard Test Methods for Tension Testing of Metallic Materials 1," *Astm*, no. C, pp. 1–27, 2009.

[58] W. Callister and D. Rethwisch, *Materials science and engineering: an introduction*, vol. 94. 2007.

[59] S.-H. Kim, E. Jeon, and D. Kwon, "Determining Brinell Hardness From Analysis of Indentation Load-Depth Curve Without Optical Measurement," *J. Eng. Mater. Technol.*, vol. 127, no. 1, p. 154, 2005.